Kent Academic Repository

Downloaded from

The version of record is available from

This document version

DOI for this version

Licence for this version

Additional information

Versions of research works

Versions of Record

Author Accepted Manuscripts

Enquiries

A global view on star formation: The GLOSTAR Galactic plane survey. XI. Radio source catalog IV: $2° < ℓ < 28°$, $36° < ℓ < 60°$ and $|b| < 1°$ [*]

S.-N. X. Medina[1,2][**], S. A. Dzib[2], J. S. Urquhart[3], A. Y. Yang[4,5], A. Brunthaler[2], K. M. Menten[2], F. Wyrowski[2], W. D. Cotton[6], A. Cheema[2], R. Dokara[2], Y. Gong[2], S. Khan[2], H. Nguyen[2], G. N. Ortiz-León[7,2], M. R. Rugel[2,6,8], V. S. Veena[2,9], H. Beuther[10], T. Csengeri[11], J. D. Pandian[12], N. Roy[13]

[1] German Aerospace Center, Scientific Information, 51147 Cologne, Germany
[2] Max-Planck-Institut für Radioastronomie, Auf dem Hügel 69, D-53121 Bonn, Germany
[3] Centre for Astrophysics and Planetary Science, University of Kent, Canterbury, CT2 7NH, UK
[4] National Astronomical Observatories, Chinese Academy of Sciences, A20 Datun Road, Chaoyang District, Beijing, 100101, P. R. China
[5] Key Laboratory of Radio Astronomy and Technology, Chinese Academy of Sciences, A20 Datun Road, Chaoyang District, Beijing, 100101, P. R. China
[6] National Radio Astronomy Observatory, 520 Edgemont Road, Charlottesville, VA 22903, USA
[7] Instituto Nacional de Astrofísica, Óptica y Electrónica, Apartado Postal 51 y 216, 72000 Puebla, Mexico
[8] Center for Astrophysics | Harvard & Smithsonian, 60 Garden St., Cambridge, MA 02138, USA
[9] I. Physikalisches Institut, Universität zu Köln, Zülpicher Str. 77, 50937 Köln, Germany
[10] Max Planck Institute for Astronomy, Koenigstuhl 17, 69117 Heidelberg, Germany
[11] Laboratoire d'astrophysique de Bordeaux, Univ. Bordeaux, CNRS, B18N, allée Geoffroy Saint-Hilaire, 33615 Pessac, France
[12] Department of Earth & Space Sciences, Indian Institute of Space Science and Technology, Trivandrum 695547, India
[13] Department of Physics, Indian Institute of Science, Bangalore 560012, India

ABSTRACT

Context. The GLOSTAR survey studies star formation with the Very Large Array (VLA) and the Effelsberg 100 meter radio telescope in the Galactic plane between $-2° < ℓ < 60°$ and $|b| < 1°$, and the Cygnus X region ($76° < ℓ < 83°$ and $-1° < b < 2°$) with unprecedented sensitivity in both flux density ($1σ$ $\sim 50\,\mu$Jy beam^{-1}) and the capability of detecting emission with angular scales in the range from $1.''0$ to the largest radio structures in the Galaxy on the order of a few degrees size.
Aims. Here, we provide a complete GLOSTAR-VLA D-configuration radio source catalog for the covered part of the Galactic disk. A catalog for the "pilot region" between $28° < ℓ < 36°$ has been published in a previous paper and here we present the complementary catalog for the area within $2° < ℓ < 28°$, $36° < ℓ < 60°$ and $|b| < 1°$.
Methods. Observations were taken with the VLA in a $4 - 8$ GHz band to image 100 square degrees of the inner Galactic disk at a reference frequency of 5.8 GHz, using a total of 260 hours of telescope time. We determined spectral indices ($α$; $S_ν \propto ν^α$) inside the observed band and in the frequency range $1.4 - 5.8$ GHz by complementing our results with those from the THOR survey, which covers $1 - 2$ GHz.
Results. The final images have an angular resolution of $18''$ and an average sensitivity of $123\,\mu$Jy beam^{-1}. The sensitivity is better ($\sim 60\,\mu$Jy beam^{-1}) in areas free of extended emission. The complementary Galactic disk catalog, presented in this work, consists of 11 211 radio sources. Of these, 1 965 are known large-scale structure sources such as star-forming region complexes, well-known supernova remnants (SNRs), SNR candidates or parts thereof. The remaining 9 227 are discrete individual sources. Source parameters, namely flux densities, sizes, spectral indices, and classifications are reported. We identify 769 H II region candidates, 359 of which are newly classified as such. The mean value of spectral indices of 225 H II regions is +0.14 ± 0.02, consistent with most of them emitting optically thin thermal radio emission. Combining our results with the previously published catalog of the pilot region, the final GLOSTAR-VLA D-configuration catalog contains 12 981 radio sources.

Key words. Star formation: high mass — radio survey — catalogs — techniques: interferometric — radio continuum: general

1. Introduction

The wide-field radio continuum surveys have been fundamental in significantly increasing the number of known radio objects, particularly sources representing high-mass young stellar objects still embedded in or close to dense gas. These objects, when far away in the Galactic plane, are typically obscured by large volumes of dust, making observations of stars in the earliest evolutionary stages difficult (see a review in high-mass star formation by Motte et al. 2018). Therefore, the GLObal view of the STAR formation in the Milky Way (GLOSTAR)[1] survey

---

[*] The full version of Table 7, and Fig. 1 are only available in electronic form at the CDS via anonymous ftp to cdsarc.u-strasbg.fr (130.79.125.5) or via `https://glostar.mpifr-bonn.mpg.de`
[**] E-mail: smedina@mpifr-bonn.mpg.de

[1] https://glostar.mpifr-bonn.mpg.de/glostar/

(Medina et al. 2019; Brunthaler et al. 2021) focuses on finding and characterizing star-forming regions in the Galactic plane at radio frequencies with unprecedented sensitivity using the *Karl G. Jansky* Very Large Array (VLA) and the Effelsberg 100 meter telescope. The GLOSTAR survey detects tell-tale tracers of star formation: compact, ultra- and hyper-compact H II regions and class II methanol masers that trace different stages of early stellar evolution. The capabilities of the GLOSTAR survey helps to locate the center of early stages of star-forming activity and complements previous radio surveys like MAGPIS, CORNISH, and THOR (Helfand et al. 2006; Hoare et al. 2012; Beuther et al. 2016) that have also largely contributed to star formation studies. Furthermore, the sensitivity achieved by GLOSTAR will highly increase and confirm the number of known sources within the Galactic plane.

To achieve its goal, the GLOSTAR survey covers a large area of the Galactic plane within 145 deg^2, covering $-2° < \ell < 60°$; $|b| < 1°$, which includes the Galactic center, and, in addition, the Cygnus X region ($76° < \ell < 83°$; $-1° < b < 2°$). It uses the results of complementary set of observations with the VLA of the NRAO[2] and the Effelsberg 100 m telescope. With this combination, the GLOSTAR survey can detect compact radio sources and recover extended emission. The GLOSTAR-VLA observations used the wideband C-band (4–8 GHz) receivers. They were performed using both the compact D-configuration (as well as complementary DnC- and C-configurations) and the extended B-configuration (as well as complementary BnA- and A-configurations) to obtain good surface brightness sensitivity and a range of resolutions to map the radio emission over a large range of angular scales. The C-band also comprises the frequency of the prominent class II CH$_3$OH (methanol) maser line (6.668 GHz), the 4.829 GHz transition line H$_2$CO (formaldehyde), and several radio recombination lines (RRLs), spectrally resolved data have also been taken within the GLOSTAR survey.

The series of GLOSTAR survey results can be found in a series of publications, starting with the first catalog of radio continuum sources by Medina et al. (2019) based on the VLA D-configuration data of the GLOSTAR "pilot region" (defined within the following limits: $28° < \ell < 36°$ and $|b| < 1°$). The overview of the GLOSTAR survey is presented by Brunthaler et al. (2021), who additionally provided examples of the combination of the VLA and the Effelsberg observations. At the same time, Dokara et al. (2021) presented a study of Galactic SNRs, Nguyen et al. (2021) presented radio continuum detections of young stellar objects (YSOs) in the Galactic center, and Ortiz-León et al. (2021) reported 6.7 GHz methanol maser detections in the Cygnus X region, followed by Nguyen et al. (2022) who reported methanol maser detections within $-2° < \ell < 60°$ and $|b| < 1°$. The GLOSTAR VLA B-configuration data were used by Dzib et al. (2023) to provide the first radio source catalog of compact sources in the pilot region and by Yang et al. (2023) for the region within $2° < \ell < 28°$, $36° < \ell < 40°$, $56° < \ell < 60°$ and $|b| < 1°$. Moreover, GLOSTAR VLA and Effelsberg data were recently used by Dokara et al. (2023) to analyze nonthermal synchrotron emission from SNR candidates in the GLOSTAR pilot region, by Gong et al. (2023) and a deep analysis of formaldehyde absorption in the Cygnus X region, while Khan et al. (2024) reports RRLs related to bright H II regions of the full survey.

The focus of this paper is the characterisation of continuum radio emission from GLOSTAR VLA D-configuration data (an-

gular resolution ~18″ and mean sensitivity ~128 μJy beam^{-1}) to provide a reliable catalog of radio sources with angular sizes of ~ 18″ to a few arcminutes. The work presented in this paper extends the analysis already conducted on the radio continuum map of the pilot region (Medina et al. 2019, in which we reported 1575 radio sources) to the rest of the inner Galactic disk covered by the survey. We will follow a similar set of steps to create a complete catalog of the Galactic disk covered by the GLOSTAR survey ($2° < \ell < 60°$ and $|b| < 1°$).

This paper is organized as follows: Section 2 gives a description of the observations and the obtained data. Section 3 describes the resulting image of the radio continuum emission and the method used for source extraction. Section 4 discusses the catalog construction and section 5 summarizes and discusses the catalog properties. In Section 6 we give a summary of the work and outline our main findings.

2. Observations and data reduction

The observations were performed with the VLA in the D-, DnC-, and C-configurations (see Table 1). The hybrid DnC configuration was preferred for targets with low elevation (that is, $\ell < 12°$) to recover a synthesized beam similar in shape to that obtained with D-configuration observations at higher elevations. However, the use of the hybrid configurations was discontinued in 2016. To compensate for this, the regions not observed in the DnC-configuration were observed in both D- and C-configurations as suggested by NRAO[3]. Though diverse array configurations were used, for the simplicity of convention, we will refer to all these low-resolution VLA observations as the GLOSTAR VLA D-configuration observations. A detailed overview of the observing strategy, data reduction, and imaging of the observed data is given in Brunthaler et al. (2021), and more specific details on the calibration and imaging of the D-configuration data are described in Medina et al. (2019). While we refer the reader to these works for details, a summary is provided below.
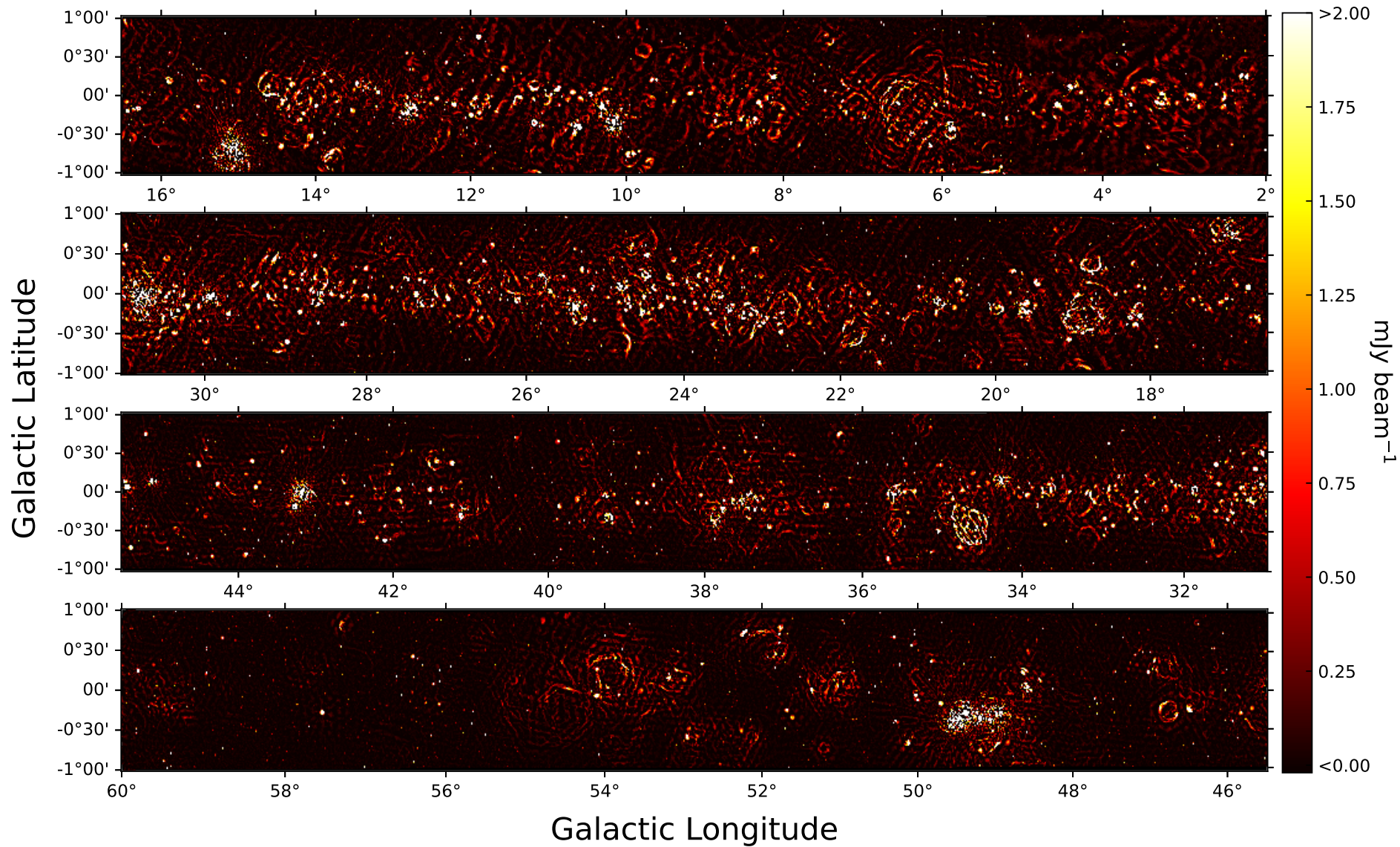
The observed band corresponds to the so-called C-band, covering a frequency range from 4.0 to 8.0 GHz. In particular, the correlator was tuned to record two 1.0 GHz wide sub-bands centered at 4.7 and 6.9 GHz in a semi-continuum mode[4]. The portion of the Galactic disk for which results are reported in this paper has a size of 100 square degrees and is delimited by $|b| \leq 1°$ and $2° \leq \ell \leq 28°$ and $36° \leq \ell \leq 60°$. The results for the areas corresponding to the Galactic center region ($-2° < \ell < +2°$) and the Cygnus X region are not included in this work and are left for future GLOSTAR catalog releases. A total of 52 observing sessions were performed to cover smaller areas using the hexagonal mosaicing scheme of pointed observations (Medina et al. 2019; Brunthaler et al. 2021)[5].

---

[2] The National Radio Astronomy Observatory is operated by Associated Universities Inc. under cooperative agreement with the National Science Foundation.

[3] `https://science.nrao.edu/facilities/vla/docs/manuals/propvla/array_configs`

[4] The observations also comprised additional high spectral resolution correlation setups covering spectral lines (see Brunthaler et al. 2021). In this paper, however, we focus on the continuum data.

[5] Note that the values given for the spacing and primary beam size in Sect. 2.1 of Medina et al. (2019) have incorrect units; they were given in arcseconds, whereas the correct units should be arcminutes. The hexagonal grid spacing is $\theta_{hex} = 3'.25$ and the FWHM primary beam size at the higher frequency band, 6.9 GHz, is $\theta_B = 45/(\nu \, [\text{GHz}]) = 6'.5$.

Fig. 1. Full GLOSTAR radio continuum map at 5.8 GHz of 116 square degrees of the Galactic disk plane ($2° < \ell < 60°$ and $|b| < 1°$). Though the most significant peak emission has a brightness of ~ 10 Jy beam^{-1}, we have constrained the contrast by choosing an upper limit of 2 mJy beam^{-1}, in order to make most of the weak extended and compact sources recognizable.

The sessions observed while the VLA was in its D- and DnC-configurations covered rectangular areas with sizes of two degrees in Galactic latitude direction and one degree in Galactic longitude direction, using ~650 target pointings (spending ~ 22 s per target pointing). C-configuration observations, on the other hand, covered 1.5 degrees in the Galactic longitude direction and observed ~950 target pointings (spending ~ 11 s per target pointing).

Quasars were observed for calibration purposes, particularly 3C 286 and 3C 48 were observed for amplitude and bandpass calibrations. A gain calibrator is observed for each session and chosen to be at an angular distance of $\lesssim 10.0°$ from the region covered in that session. The observations are part of the VLA projects with IDs 11B-168, 13A-334, 15B-175, and 17A-197. The total telescope time used for these observations is 260 hours (that is, five hours per session). The observations occurred from 2011 December to 2017 June. Individual observation dates, corresponding VLA project ID, VLA configuration, and used gain calibrators are listed in Table 1.

The data sets were edited, calibrated, and imaged using the `Obit` software package (Cotton 2008), designed for handling radio astronomical data[6]. Prior to calibration, the data sets were edited to remove the first 10 seconds of the scans on calibrators, which are affected by the antennas slewing. Then, a standard calibration is applied. This includes amplitude corrections based on the switched power signal, group delay, bandpass, amplitude and phase, and polarization calibration. The standard calibration is alternated with the editing of data affected by instrumental problems or radio frequency interference. Then, the data are reset and calibrated again, excluding the identified problematic data.

The images are produced using the `Obit` task MFImage. First, the data for every target pointing are imaged individually, covering the FWHM primary beam corresponding to the lowest continuum band, 4.7 GHz, which is 8′.4. In cases for which the target pointing covered strong sources located outside the primary beam that are bright enough to affect the imaging, we add outlier fields at the location of these sources to account for them in the cleaning process. The observed bandwidth is divided into frequency bins that are narrow enough such that the effects of variable spectral index and antenna pattern variations are minor, allowing a joint spectral deconvolution. MFImage then generates an image for each individual frequency bin, that are then weighted averaged to produce the final map of the target field. The images are produced using a Briggs' weighting with robustness parameter 0.0. Finally, the frequency bins and the weighted averaged map are combined to produce the mosaiced images with a restoring beam of 18″ and a pixel size of 2″.5 as described by Medina et al. (2019) and Brunthaler et al. (2021). The shortest baseline of the VLA in the D-configuration is 35 m. Thus, sources with angular sizes larger than ~ 4′ are filtered out from the images. In order to conserve computational resources, the total observed area was divided into 6 sub-mosaics that constitute the final radio continuum map. The full continuum image of the Galactic disk area covered by the GLOSTARS survey, $2° < \ell < 60°$ and $|b| < 1°$ (i.e., including the pilot region), is shown in Figure 1.

Table 1. All observed epochs of the GLOSTAR-VLA survey presented in this work.

ℓ (°) range	VLA Project ID	Date of Obs. dd/mm/yyyy	VLA Conf.	Phase calibrator
02 – 03	15B-175	17/01/2016	DnC	J1820–2528
03 – 04	15B-175	21/01/2016	DnC	J1820–2528
04 – 05	15B-175	22/01/2016	DnC	J1820–2528
05 – 06	15B-175	16/01/2016	DnC	J1820–2528
06 – 07	17A-197	03/04/2017	D	J1820–2528
06 – 7.5	17A-197	31/05/2017	C	J1820–2528
07 – 08	17A-197	31/03/2017	D	J1820–2528
08 – 09	17A-197	21/02/2017	D	J1820–2528
7.5 – 09	17A-197	05/06/2017	C	J1820–2528
09 – 10	15B-175	24/01/2016	DnC	J1820–2528
10 – 11	13A-334	16/05/2013	DnC	J1820–2528
11 – 12	13A-334	17/05/2013	DnC	J1820–2528
12 – 13	17A-197	03/03/2017	D	J1825–0737
13 – 14	17A-197	04/04/2017	D	J1825–0737
14 – 15	17A-197	19/02/2017	D	J1825–0737
15 – 16	14A-420	14/07/2014	D	J1825–0737
16 – 17	14A-420	24/07/2014	D	J1825–0737
17 – 18	14A-420	05/08/2014	D	J1825–0737
18 – 19	14A-420	14/08/2014	D	J1825–0737
19 – 20	14A-420	12/07/2014	D	J1825–0737
20 – 21	14A-420	23/07/2014	D	J1825–0737
21 – 22	14A-420	28/07/2014	D	J1825–0737
22 – 23	14A-420	27/07/2014	D	J1825–0737
23 – 24	14A-420	26/08/2014	D	J1825–0737
24 – 25	14A-420	16/07/2014	D	J1825–0737
25 – 26	14A-420	29/07/2014	D	J1825–0737
26 – 27	14A-420	13/08/2014	D	J1825–0737
27 – 28	14A-420	28/08/2014	D	J1825–0737
36 – 37	14A-420	07/07/2014	D	J1907+0127
37 – 38	14A-420	04/07/2014	D	J1907+0127
38 – 39	14A-420	01/08/2014	D	J1907+0127
39 – 40	14A-420	25/08/2014	D	J1907+0127
40 – 41	14A-420	07/08/2014	D	J1907+0127
41 – 42	14A-420	02/07/2014	D	J1907+0127
42 – 43	14A-420	09/07/2014	D	J1907+0127
43 – 44	14A-420	17/07/2014	D	J1907+0127
44 – 45	14A-420	03/08/2014	D	J1907+0127
45 – 46	14A-420	29/06/2014	D	J1907+0127
46 – 47	15B-175	25/11/2015	D	J1922+1530
47 – 48	15B-175	13/11/2015	D	J1922+1530
48 – 49	15B-175	21/11/2015	D	J1922+1530
49 – 50	15B-175	14/11/2015	D	J1922+1530
50 – 51	15B-175	22/11/2015	D	J1922+1530
51 – 52	15B-175	11/11/2015	D	J1922+1530
52 – 53	15B-175	20/11/2015	D	J1922+1530
53 – 54	15B-175	10/11/2015	D	J1922+1530
54 – 55	15B-175	27/11/2015	D	J1922+1530
55 – 56	15B-175	17/12/2015	D	J1922+1530
56 – 57	15B-175	28/11/2015	D	J1925+2106
57 – 58	15B-175	08/11/2015	D	J1925+2106
58 – 59	11B-168	15/12/2011	D	J1931+2243
59 – 60	11B-168	29/12/2011	D	J1931+2243

3. Analysis of the continuum map

3.1. Radio Continuum Map

The observational data previously described were used to image 100 square degrees of the Galactic plane by producing six sub-mosaics (see Table 2 for each longitude range, including the pilot region). Together with the sub-mosaic of the pilot region, previously reported by Medina et al. (2019), we have a complete map of 116 square degrees of the Galactic plane (that is,

Table 2. Average noise values estimated for the 7 mosaic maps produced of the survey area across the full GLOSTAR radio map.

Galactic longitude range	σ_{rms} [μJy beam^{-1}]	Radio sources	LSS
$2° - 12°$	171	2026	31
$12° - 20°$	165	1655	19
$20° - 28°$	157	1888	29
$28° - 36°$ [*]	150	1770 [**]	27
$36° - 44°$	119	1756	8
$44° - 52°$	98	1766	13
$52° - 60°$	84	2120	5
$2° - 28°$; $36° - 60°$ [***]	123	11211	106
$2° - 60°$	123	12981	132

[*] Corresponding to the pilot region, previously reported by Medina et al. (2019). [**] This number includes 195 sources related to the 27 LSS, as well as the 1575 individual sources. [***] This work.


Fig. 2. Noise distribution of the full GLOSTAR VLA D-configuration mosaic. The range of pixel values ranges between -2 and 2 mJy. The red line shows the results of a Gaussian fit to the distribution, $\sigma_{rms} = 123\,\mu$Jy beam^{-1}. The bin size is $50\,\mu$Jy beam^{-1}.

$2° < \ell < 60°$ and $|b| < 1°$). Figure 1 presents the radio continuum map of the complete region produced from the D, DnC, and C-configuration data. This radio map has an effective central frequency of 5.8 GHz and has been restored using a circular beam of 18″. Although the observed region extends slightly beyond $|b| = 1.0°$, the noise increases significantly in these outer regions because of the primary beam attenuation and because these areas do not overlap with other pointings. Hence, sources detected beyond this latitude range have been excluded from the analysis presented here, although they are listed in our final catalog.

Inspection of Fig. 1 reveals the presence of thousands of compact sources and many large-scale sources (LSSs, see Sect. 3.2 for details) associated, for example, with prominent star-forming complexes (e.g., W31, W33, W49, and W51) or supernova remnants (e.g., W28 and W44). The emission towards these more complex regions is not fully recovered due to the lack of short (u, v) baselines, which also results in strong negative bowls that affect the noise level around them. Therefore, these LSSs cause significantly higher noise levels in the Galactic mid-plane and the inner part of the Galactic disk, where they are more densely concentrated, and affect the quality of the imaging around them. This is demonstrated in Table 2 where the mean noise values determined from each of the mosaics can be seen to decrease with longitude from the Galactic center to the outer part of the disk where less star formation is occurring. In Fig. 2 we present a histogram of the pixel values from the whole survey region. The significant noise variations across the GLOSTAR VLA D-configuration map produce the non-Gaussian profile of the pixel noise values. We use a Gaussian fit to this pixel distribution to estimate the overall sensitivity of the final map. The standard deviation of the distribution of the pixel values, σ_{rms}, is $123\,\mu$Jy beam^{-1}; however, the noise values can be significantly higher towards prominent complexes concentrated towards the mid-plane. The noise level in regions free of extended emission is approximately $60\,\mu$Jy beam^{-1}.

3.2. Source extraction

The range of detected structures, level of complexity, variation, and survey coverage make source extraction and analysis difficult in the GLOSTAR low-resolution images presented here. In our previous analysis of the pilot region, we developed a number of steps to automatically identify sources and confirm them visually and by spatially correlating them with published source
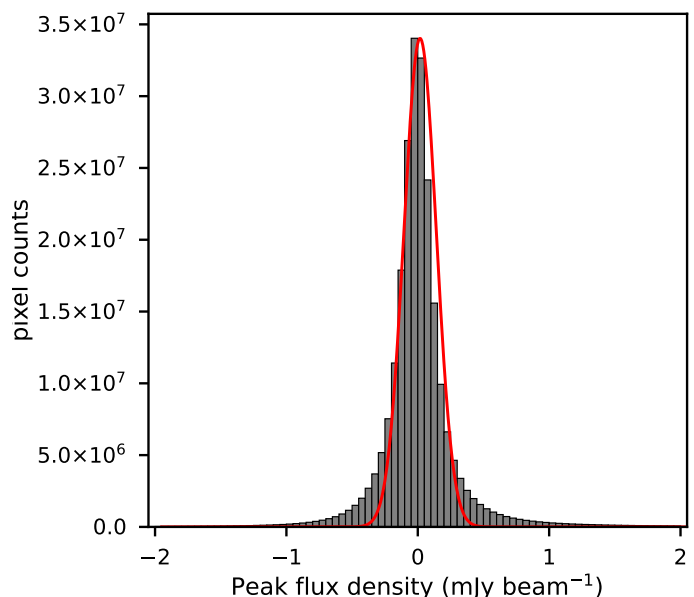
catalogs at different wavelengths (Medina et al. 2019). In this paper, we will follow the same process to create a catalog of radio sources for the rest of the covered Galactic plane, which will then be combined with the sources detected in the pilot field to create a complete catalog of radio sources in the GLOSTAR VLA D-configuration radio map (excluding the Galactic center and the Cygnus X regions); that is $2° < \ell < 60°$ and $|b| < 1°$. We have again used the `BLOBCAT` software package to perform the source extraction; see Hales et al. (2012) for a detailed description of this Python code. This code has also been previously used for the source extraction of a complementary 21 cm radio continuum survey (The HI/OH/Recombination line survey of the inner Milky Way (THOR); Beuther et al. 2016; Wang et al. 2018), which will facilitate further comparisons. Below we provide a brief outline of the method used and refer the reader to Medina et al. (2019) for more details. The methodology steps are also visualized in Fig. 3.

Creation of the noise maps. To perform the automatic source extraction, we first need to produce an independent noise map of the region due to the position-dependent nature of the noise in GLOSTAR VLA D-configuration radio continuum maps. We use the *rms* estimation algorithm within the SExtractor package (Bertin & Arnouts 1996; Holwerda 2005). This algorithm defines the *rms* value for each pixel in an image by determining the distribution of pixel values within a local mesh until all values are around a chosen sigma value. Following our previous work Medina et al. (2019), for the calculations we used a detection and analysis threshold of 5σ, a minimum size of 5 pixels, and a mesh size of 80×80 pixels^2. As a result, most real emission is removed from the noise image, and the determined noise map represents the correct noise level.

Automatic source extraction with `BLOBCAT`. We employ the `BLOBCAT` software package that uses an algorithm to detect and identify blobs, or islands of pixels representing sources, in two-dimensional astronomical radio-wavelength images (see Hales et al. 2012, for details). The algorithm makes a pixel-by-pixel comparison between the main image and the background noise
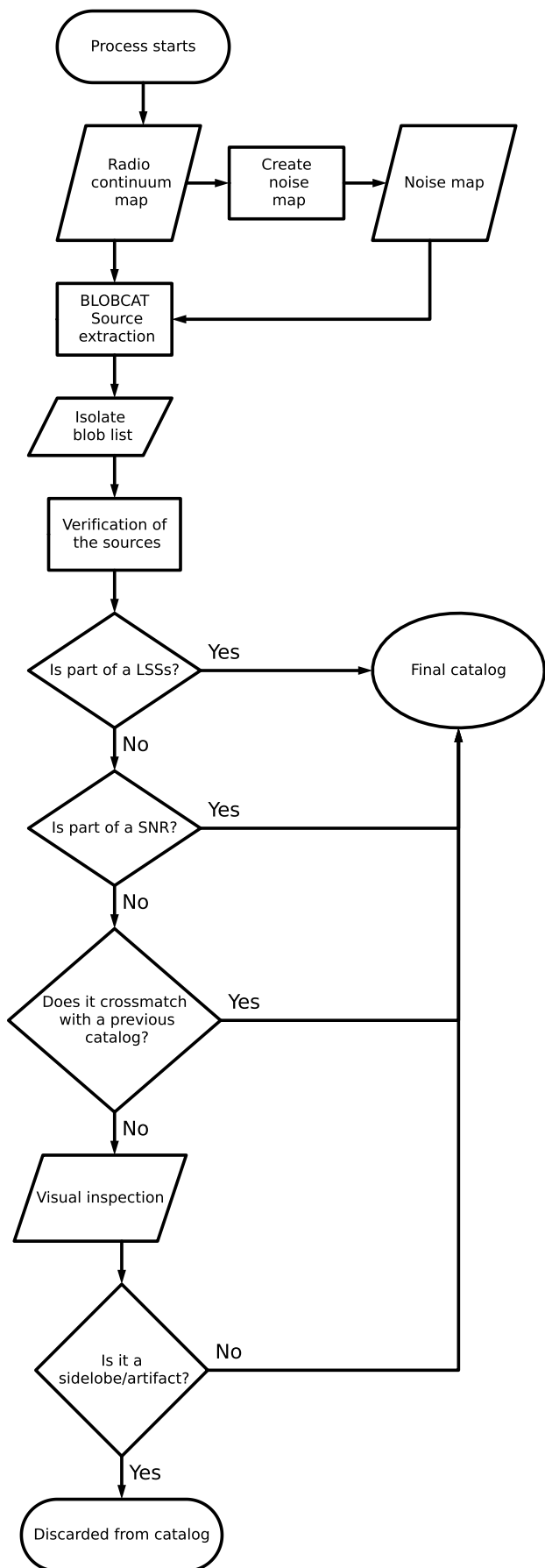
Fig. 3. Methodology of the source extraction and verification followed for the GLOSTAR-VLA survey data to create the final catalog.

map, locates pixels above a given threshold, and defines "blobs" around these pixels. Then, a first source parameter set is obtained by fitting a 2D elliptical Gaussian. Later, the peak and integrated flux densities are corrected by considering biases from the Gaussian fits, such as source morphology (see Hales et al. 2012, for details). BLOBCAT returns several parameters from which we use the following (and their corresponding errors) for our catalog construction: the 2D source position (RA_p and Dec_p; notice these are software internal names and not the image coordinate system), peak flux density (S_p_CBBWS), integrated flux density (S_int_CB), and the number of pixels covered by the source (npix).

Following our previous work, we applied a detection threshold (dSNR) of 4σ and a minimum source size of 5 pixels in diameter ($\sim13''$). This resulted in the extraction of 13 001 blobs potentially associated with radio sources in the area delimited by $2° < \ell < 28°$, $36° < \ell < 60°$ and $|b| < 1°$. All of them have flux above four times that in the local noise map and have a size comparable to or larger than the beam. However, this sample contains a significant number of artifacts that need to be removed, and also emission from large-scale structures, that is, sources fragmenting into multiple components that need to be grouped. Furthermore, at the edges of the map, the noise increases significantly, therefore, the sources located at $|b| > 1°$ are excluded from further analysis and their identification names are marked with an $\ast$. The following steps will address these issues. Additionally, in our previous work, we also flagged (that is labeled) sources that appeared to consist of two or more distinct emission peaks; however, in this work, we have not attempted to flag them or to separate the emission because in our previous work, only around 3% of the sources are affected by this problem, and those are resolved in the GLOSTAR VLA B-configuration images (e.g., Dzib et al. 2023). Finally, as in our previous works (e.g., Medina et al. 2019), we considered the Y-factor ($Y_{factor} = S_{\nu,Int}/S_{\nu,Peak}$) and roughly divided the sources into extended ($Y_{factor} > 2.0$), compact ($1.2 < Y_{factor} \leq 2.0$) and unresolved ($Y_{factor} \leq 1.2$).

Identification of Large Scale Structures (LSSs). In our previous work, we defined LSSs as over-resolved structures whose emission is broken up into multiple independent fragments of radio sources. To identify LSSs, we performed a visual inspection and compared the radio emission distribution with their corresponding 8.0 μm maps extracted from the GLIMPSE archive. Most GLOSTAR sources with corresponding 8.0 μm have thermal radio emission, that is they are H II regions. SNRs are also generally faint or even not detected at mid-infrared wavelengths (Dokara et al. 2021). In Fig. 4 we show some examples of these LSSs. We delimited a rectangular area around the coherent infrared structures morphologically correlated with the radio emission (see the left panel of Fig. 4). Also, we have delimited a rectangular area around radio emission sources with shell-like morphology that are clearly part of one source even if there is no clear correlation with the 8.0 μm emission, which is the case for many SNRs (see the lower right panel of Fig. 4). Finally, we also classified as LSSs the complexes with two or more independent sources that clearly belong to the same star-forming region as seen in the 8.0 μm maps (see the top right panel of Fig. 4). All extended radio sources in these boxed regions are considered to be part of one LSS. Individual fragment components and their properties are given in the catalog, however, they have been excluded from the statistical analysis presented here. Compact and unresolved radio sources that are considered unlikely to be associated with LSSs have been retained in the final catalog as distinct sources, since these are possible individual sources
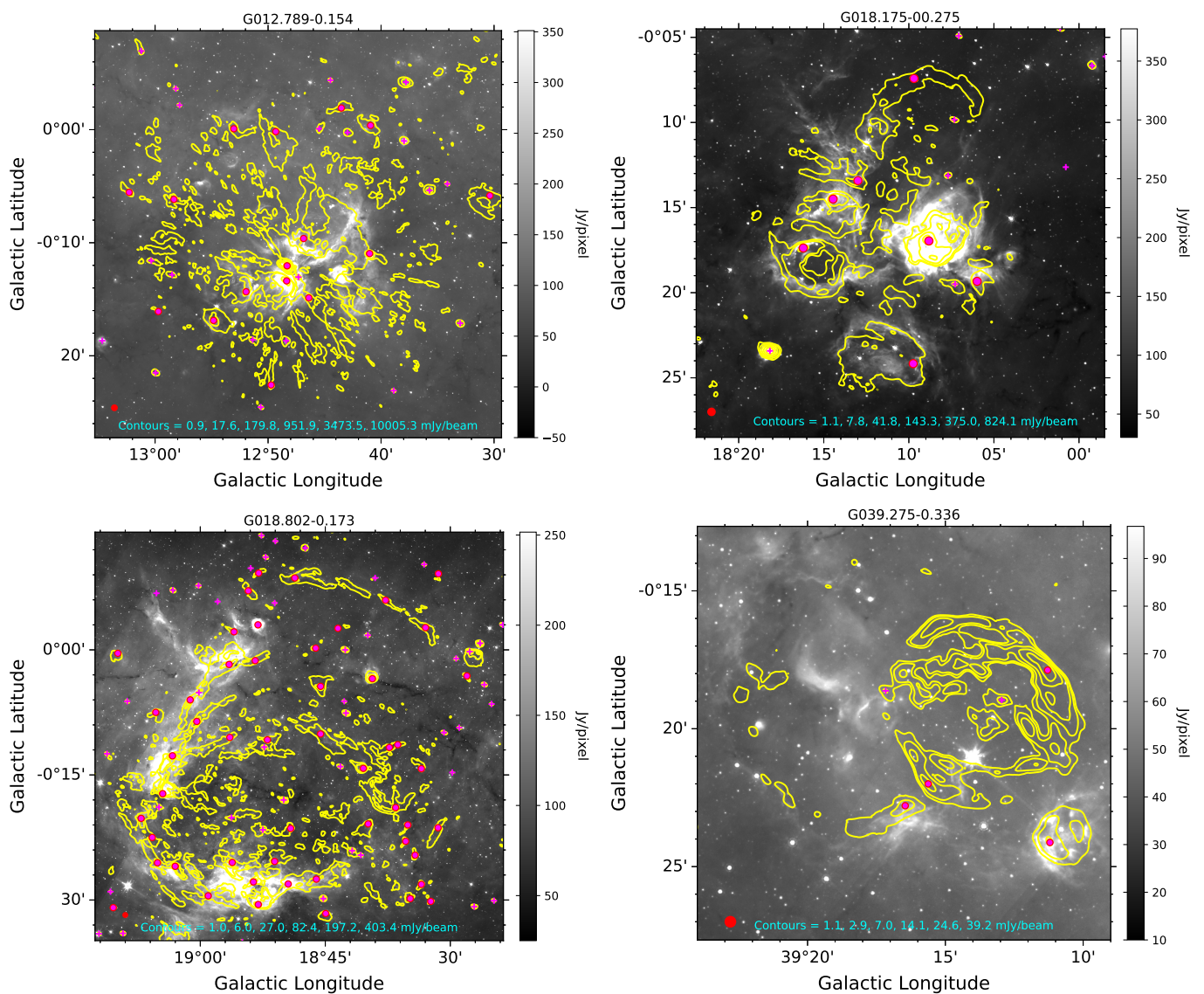
Fig. 4. Examples of radio emission associated with large-scale structures. The grey scale background represents GLIMPSE $8\,\mu$m emission, while the yellow contours are the GLOSTAR 5.8 GHz radio continuum emission. These regions often show coherent infrared structures that are morphologically correlated with most of the radio emission (see examples presented in the upper panels). Although this correlation is not always present, the different radio emission blobs are clearly related with each other (see examples presented in the lower panels). The contours are determined as described in the figures, and the red-filled circle shown in the lower left corners shows the GLOSTAR VLA D-configuration beam FWHM. The magenta-filled circles indicate the peak positions of radio sources associated with these regions, and magenta crosses indicate compact radio sources in the area that are treated as separate sources.

and not part of the extended emission. They are included in our further analysis.

In this work, we have visually identified a total of 106 large-scale radio emission regions containing 839 individual fragments within $2° < \ell < 28°$, $36° < \ell < 60°$ and $|b| < 1°$, which includes the SNRs like W28, W30, and W49 (e.g., Green 2019) and star-forming region complexes such as W31 (Ghosh et al. 1989), W33 (Messineo et al. 2011), M16 (Oliveira 2008), M17 (Chini & Hoffmeister 2008), W39 (Kerton et al. 2013), and W51 (Ginsburg et al. 2017).

In Table 3, we give the list of LSSs, including the 27 from the pilot region. The name of each structure has been constructed from the central coordinates of the enclosing box. The table includes the extent of the boxed region in ℓ and b and the integrated flux of the total emission in the box minus the emission from any compact sources that are considered as distinct sources. The to-

tal integrated flux density of each LSS, is calculated by adding the flux densities of all components together. The measured parameters of LSSs should be used with caution as the flux densities and sizes are unlikely to correspond to discrete sources, but rather to source complexes. We also point the readers to Dokara et al. (2021) and Dokara et al. (2023) for a discussion on the calculation of flux densities of sources identified as SNRs.

Crossmatch with recently identified SNR candidates. SNRs are sources of nonthermal radio emission (Anderson et al. 2017) that can also be detected with the GLOSTAR observations (see Medina et al. 2019; Dokara et al. 2021, 2023). The radio emission from most of these radio sources is extended and, in many cases, has a weak surface brightness. Because of these properties, automatic source extraction is not optimal to fully recover these sources. Their identification and total flux determination require a more detailed visual inspection that goes beyond the

Table 3. Large scale structure sources.

Name	ℓ_{min} (°)	ℓ_{max} (°)	b_{min} (°)	b_{max} (°)	Int flux (Jy)	Name	ℓ_{min} (°)	ℓ_{max} (°)	b_{min} (°)	b_{max} (°)	Int flux (Jy)
G002.273+00.233	2.2022	2.3444	0.1851	0.2809	0.876	G024.782+00.083	24.6712	24.8938	−0.0231	0.1899	3.130
G003.020−00.831	2.6983	3.3427	−1.0227	−0.6386	0.413	G025.376−00.210 (W42)	25.1914	25.5599	−0.4167	−0.0030	14.304
G003.264−00.059	3.1428	3.3843	−0.1798	0.0624	2.054	G025.571+00.208	25.4747	25.6664	0.1571	0.2598	0.428
G003.431+00.169	3.3031	3.5599	0.1174	0.2205	0.285	G025.867+00.132	25.7329	26.0002	−0.0196	0.2839	1.769
G003.784−00.278*	3.6846	3.8840	−0.4004	−0.1557	0.351	G026.123+00.021**	25.9820	26.2630	−0.0301	0.0725	0.260
G003.930−00.072	3.8559	4.0048	−0.1254	−0.0180	0.416	G026.511−00.371	26.3833	26.6394	−0.4873	−0.2551	0.305
G004.382+00.125	4.2975	4.4671	0.0245	0.2253	1.399	G027.240−00.108**	27.1052	27.3742	−0.1894	−0.0275	0.975
G005.151−00.321	5.0827	5.2202	−0.4099	−0.2319	0.529	G027.301+00.265	27.2457	27.3555	0.2408	0.2901	0.085
G005.346+00.104	5.2181	5.4741	−0.0436	0.2520	0.156	G027.395−00.008*	27.3435	27.4462	−0.0489	0.0337	0.804
G005.351−00.976	5.1610	5.5414	−1.0161	−0.9357	0.645	G027.497+00.191	27.4427	27.5518	0.1595	0.2235	0.781
G005.886−00.453 (W28)	5.7897	5.9815	−0.6064	−0.3000	8.493	G027.504−00.115	27.4122	27.5952	−0.2009	−0.0291	0.168
G006.430−00.218*	6.0130	6.8468	−0.6657	0.2295	5.051	G036.705−00.175**	36.5630	36.8467	−0.2978	−0.0518	0.184
G007.113−00.138*	6.9050	7.3214	−0.3177	0.0418	0.734	G036.886+00.475**	36.7968	36.9760	0.4294	0.5202	0.124
G007.420+00.710	7.3358	7.5032	0.6228	0.7978	0.274	G037.855+00.319**	37.6403	38.0700	0.0971	0.5416	0.667
G008.134+00.239 (W30)	7.9896	8.2776	0.1119	0.3667	5.097	G039.275−00.336*	39.1547	39.3947	−0.4261	−0.2462	1.132
G008.159−00.121 (W30)	7.9677	8.3505	−0.1932	−0.0489	0.764	G041.087−00.213	41.0224	41.1522	−0.2500	−0.1760	0.296
G008.343−00.317 (W30)	8.2847	8.4015	−0.3662	−0.2686	0.826	G041.479+00.408*	41.3678	41.5892	0.2722	0.5442	0.666
G008.557−00.291 (W30)	8.4830	8.6311	−0.3580	−0.2242	0.223	G043.156+00.001 (W49)	43.0275	43.2852	−0.1192	0.1211	32.464
G008.838−00.310 (W30)	8.6346	9.0410	−0.4385	−0.1816	2.070	G043.421+00.556	43.3305	43.5112	0.4884	0.6243	0.153
G009.603+00.203	9.4802	9.7264	0.1173	0.2891	1.188	G044.129+00.051	43.9331	44.3240	−0.0641	0.1653	0.914
G009.679−00.078*	9.6082	9.7503	−0.1704	0.0138	0.211	G044.797−00.496	44.7431	44.8515	−0.5644	−0.4284	0.098
G009.697−00.861	9.6285	9.7648	−0.9388	−0.7840	0.271	G045.100+00.151	45.0045	45.1957	0.0653	0.2370	6.241
G009.782+00.571*	9.6491	9.9141	0.4650	0.6773	0.385	G045.453+00.083	45.2807	45.6244	−0.0524	0.2177	7.326
G009.949−00.809*	9.8684	10.0300	−0.9148	−0.7034	1.101	G045.644−00.439*	45.4986	45.7898	−0.5602	−0.3175	0.169
G010.094−00.306	9.7930	10.3944	−0.5601	−0.0509	28.705	G046.205+00.017**	46.1323	46.2778	−0.0698	0.1028	0.039
G010.642−00.393 (W31)	10.5689	10.7153	−0.4431	−0.3432	5.594	G046.388+00.880	46.3046	46.4717	0.8094	0.9497	0.083
G011.181−00.348*	11.1308	11.2306	−0.3936	−0.3018	1.957	G046.763−00.272*	46.6174	46.9084	−0.4204	−0.1237	0.719
G011.184+00.128	11.0846	11.2825	0.0497	0.2053	0.777	G046.771+00.257	46.6066	46.9354	0.0866	0.4265	0.324
G011.194−00.687	11.1459	11.2415	−0.7555	−0.6180	0.095	G048.597+00.036	48.5073	48.6868	−0.0476	0.1189	2.242
G011.386−00.060*	11.3002	11.4722	−0.1233	0.0038	0.771	G048.630+00.243	48.5466	48.7136	0.1891	0.2970	0.632
G011.902−00.141	11.7201	12.0838	−0.3116	0.0300	3.402	G049.341−00.462 (W51)	48.8824	49.7988	−0.8138	−0.1105	72.024
G012.789−00.154 (W33)	12.4841	13.0933	−0.4020	0.0936	27.244	G051.084+00.016	50.7336	51.4349	−0.2626	0.2946	1.315
G013.445+00.146*	13.3955	13.4942	0.0943	0.1976	0.437	G051.203−00.753	51.1109	51.2943	−0.8542	−0.6516	0.150
G013.644+00.252	13.5986	13.6898	0.2122	0.2919	0.068	G051.926+00.567	51.6540	52.1973	0.3706	0.7628	1.025
G013.732−00.026	13.6419	13.8220	−0.1202	0.0688	0.169	G052.860−00.527	52.7256	52.9947	−0.6574	−0.3974	0.377
G013.787−00.843	13.5905	13.9839	−1.0315	−0.6550	1.322	G053.938+00.236	53.6859	54.1899	0.0142	0.4575	1.442
G013.987−00.133	13.9315	14.0431	−0.1734	−0.0928	0.708	G054.564−00.074	54.2844	54.8440	−0.2404	0.0922	0.241
G014.509+00.071	14.2662	14.7516	−0.1981	0.3409	3.568	G057.239+00.839*	57.1496	57.3291	0.7303	0.9475	0.185
G015.098−00.668 (M17)	14.7537	15.4420	−1.0629	−0.2741	18.100	G059.600−00.180	59.5392	59.6608	−0.2312	−0.1282	0.072
G015.665−00.212	15.5952	15.7341	−0.2672	−0.1567	0.094	Pilot Region (Medina et al. 2019):					
G016.664−00.338	16.5305	16.7973	−0.4606	−0.2155	0.447	G028.026−00.045	27.970	28.082	-0.100	0.010	0.32
G016.920+00.832 (M16)	16.1891	17.6513	0.5999	1.0636	2.881	G028.520+00.132	28.470	28.570	0.049	0.215	0.30
G017.478−00.114*	17.3969	17.5591	−0.1994	−0.0285	0.183	G028.6−00.1 (SNR)*	28.544	28.694	-0.188	-0.038	0.95
G017.796−00.029**	17.7099	17.8825	−0.1043	0.0458	0.079	G029.087−00.682	28.976	29.199	-0.756	-0.608	0.22
G018.175−00.275	18.0359	18.3139	−0.4474	−0.1033	5.957	G029.219+00.415	29.095	29.343	0.344	0.486	0.50
G018.772+00.417*	18.6292	18.9155	0.2781	0.5559	2.154	G029.6+00.1 (SNR)*	29.512	29.612	0.071	0.165	0.13
G018.802−00.173 (W39)	18.4183	19.1855	−0.5303	0.1836	7.595	W43−south center	29.805	30.131	-0.195	0.071	9.08
G018.840−00.934*	18.6930	19.2028	−1.0442	−0.8241	0.631	G029.986−00.582	29.913	30.060	-0.650	-0.513	0.11
G019.621−00.224	19.4219	19.8206	−0.3935	−0.0536	6.335	G030.462+00.449	30.405	30.519	0.393	0.506	0.16
G019.988−00.180*	19.8842	20.0916	−0.2779	−0.0823	1.733	W43 center	30.525	30.908	-0.238	0.080	13.43
G020.485+00.181	20.4336	20.5371	0.1370	0.2245	0.332	G031.053+00.482	30.992	31.115	0.435	0.529	0.59
G020.727−00.154	20.6068	20.8465	−0.2996	−0.0075	1.837	G031.166−00.106	31.117	31.214	-0.050	-0.162	0.42
G021.023−00.469*	20.9295	21.1160	−0.5487	−0.3893	0.100	G031.411−00.234	31.355	31.467	-0.286	-0.183	0.60
G021.076−00.281	20.9225	21.2286	−0.3555	−0.2057	0.324	G031.5−00.6 (SNR)*	31.400	31.700	-0.790	-0.490	0.14
G021.553−00.098	21.5013	21.6043	−0.1442	−0.0510	0.132	G031.9+00.0 (SNR)*	31.821	31.920	-0.053	0.071	1.01
G021.633−00.237**	21.5136	21.7515	−0.3378	−0.1368	0.238	G032.4+00.1 (SNR)*	32.322	32.488	0.027	0.172	0.10
G021.810−00.515*	21.6236	21.9964	−0.7031	−0.3263	1.896	G032.586−00.172	32.534	32.637	-0.284	-0.059	0.26
G022.885−00.328	22.7114	23.0583	−0.4449	−0.2110	1.468	G032.8−00.1 (SNR)*	32.649	32.950	-0.269	0.115	0.67
G023.100+00.553	23.0305	23.1686	0.4874	0.6179	0.311	G033.179−00.010	33.118	33.240	-0.075	0.055	0.66
G023.279−00.343*	23.0626	23.4947	−0.5853	−0.1008	4.065	G033.2−00.6 (SNR)*	33.033	33.327	-0.708	-0.395	0.09
G023.575−00.046	23.4805	23.6688	−0.1478	0.0556	0.881	G033.6+00.1 (SNR)*	33.567	33.781	-0.067	0.132	0.93
G023.846−00.185**	23.8014	23.8903	−0.2344	−0.1350	0.072	G034.260+00.125	34.177	34.343	0.043	0.207	10.17
G024.186+00.233	24.1238	24.2477	0.1552	0.3108	0.443	G034.6−00.5 (SNR)*	34.390	34.930	-0.760	-0.093	2.96
G024.385+00.688	24.3285	24.4413	0.5469	0.8300	0.159	G035.032−00.283	34.994	35.070	-0.363	-0.204	0.04
G024.461+00.271	24.3315	24.5912	0.1915	0.3500	1.139	G035.506−00.026	35.316	35.696	-0.157	0.106	2.36
G024.725−00.083	24.6746	24.7749	−0.1392	−0.0266	0.567	G035.6−00.4 (SNR)*	35.502	35.692	-0.593	-0.258	2.36
G024.739−00.658*	24.6763	24.8022	−0.8330	−0.4831	0.687	G035.680−00.868	35.610	35.750	-0.943	-0.792	0.19

Notes: The LSS name is constructed from the central position of the box used to encapsulate the regions. When the LSS is known to be (part of) a well-known region, this is mentioned within brackets next to the GLOSTAR name. The sources with * and ** are associated with SNRs from the catalog of Green (2019) and SNR candidates from the catalog of Anderson et al. (2017), respectively. The values in the Int flux column are obtained by adding the flux densities of individual components as obtained from the flux extraction procedure described in Section 3.2.

scope of this work. SNRs and SNR candidates in the observed area of the GLOSTAR survey are the subject of the studies presented by Dokara et al. (2021) and Dokara et al. (2023). However, our procedure recovered sources located in the regions containing well-known SNRs and previously identified SNR candidates. Previously, well-known SNRs with large angular scales were identified as LSSs (see also Table 3). Additionally, we also identified 1 126 extended sources ($Y_{factor} > 2.0$) located in areas of other SNR candidates, including the 80 new SNR candidates from the GLOSTAR survey (Dokara et al. 2021). These sources are labeled in the final catalog.

Cross match with previous catalogs. In order to verify the remaining sources, the next step was to assume that any radio source that has a counterpart in a published radio or mid-infrared catalog is real. We used several complementary multi-wavelength surveys to cross match with our detected radio sources to identify possible counterparts. The selected surveys are better described in the following sections. They either have comparable angular resolution: GLIMPSE (Fazio et al. 2004), WISE (Wright et al. 2010), HiGAL (Molinari et al. 2010, 2016), ATLASGAL (Schuller et al. 2009), GLOSTAR VLA B-configuration (Yang et al. 2023), CORNISH (Hoare et al. 2012), RMS (Urquhart et al. 2009), and THOR (Beuther et al. 2016; Wang et al. 2020) all have angular resolutions between 6.0 and 20″. The CORNISH and RMS VLA surveys, both at 5.0 GHz, comparable to the GLOSTAR survey's wavelength, have resolutions of 1.5″ and 2″, respectively. We used an initial cross match radius of 10″, the same as chosen in our previous paper (Medina et al. 2019).

The offset distribution between GLOSTAR VLA D-configuration sources and the above catalogs was analyzed based on the empirical cumulative distribution function (ECDF), see Figure 5. The offsets between GLOSTAR and other radio centimeter wavelength surveys (THOR, CORNISH, and RMS) in Fig. 5 show a good position match. This is because they are tracing radio emission with similar morphology. For ATLASGAL, GLIMPSE, and WISE, the situation is different. ATLASGAL 870 μm submillimeter continuum sources trace compact high column density emission of cold dust (and associated molecular gas) in star-forming regions and are quite rare. Thus, a radio source the direction of an ATLASGAL source may be related to it even if the angular separation between the ATLASGAL and GLOSTAR positions is larger than 10″. The cases of the WISE and GLIMPSE catalogs are more complex: due to the high density of foreground field stars detected in these survey there is a significant probability of false line of sight matches with the GLOSTAR detections. As a precaution, a smaller matching radius of 6″ was used for WISE and GLIMPSE in our final counterpart search.

We have found 8 235 radio sources with at least one counterpart at a 10″ cross match radius. In Table 4, we summarize the counterparts of the GLOSTAR-VLA sources with the complementary multi-wavelength surveys.

Visual inspection. After our cross match analysis, we find 2 807 blobs to be unrelated to extended sources and to have no counterparts in any other survey. To understand the nature of these sources, we first compare the statistics with the expected number of false detections. As discussed in our previous works (e.g., Medina et al. 2019; Yang et al. 2023) the number of false detections can be calculated using the complementary cumulative distribution function $\Phi(x) = 1 - \phi(x)$, where $\phi(x)$ is the cumulative distribution function. Assuming that the noise in our
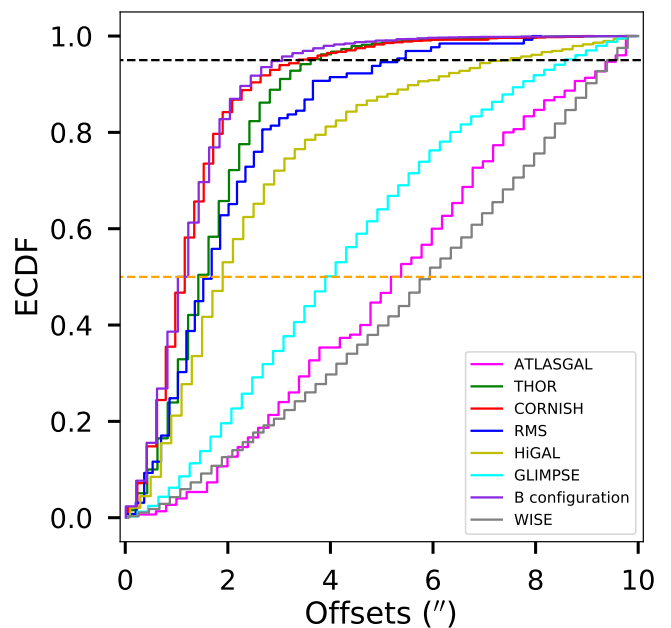
Fig. 5. Empirical cumulative density function of the position offsets among GLOSTAR compact sources (Y-factor ≤ 2.0) with the other survey counterparts. The dashed lines indicate the 50% (orange) and 95% (black) of matches.

radio maps follows a Gaussian distribution,

$$\phi(x) = \frac{1}{2}\left[1 + erf\left(\frac{x}{\sqrt{2}}\right)\right] \tag{1}$$

where erf is the error function given by

$$erf(x) = \frac{1}{\sqrt{\pi}} \int_{-x}^{x} e^{-t^2} dt. \tag{2}$$

$\Phi(x)$ is the probability that the value of a random variable x with a standard normal distribution will exceed the value x. Considering the 100 square degrees of the analyzed radio map, the expected false detection is calculated like $\theta^2 \times \phi(x)$, where θ is the synthesized beam size. Therefore, considering sources above 4σ, we expect only 127 false detections, which is much smaller than the 2 807 sources without counterparts.

Next, we carried out a visual inspection to identify and remove *side lobes* (which appear as elongated blobs in the direction of a very bright source) and *artifacts* (weak sources, between 4–5σ, and have a size much smaller than the beam size). This led to the removal of 1 790 blobs. We also identified 19 sources as *unclear*; these sources have a signal-to-noise (S/N) ratio between 4.0 and 5.0; they have no counterpart and do not comply with the characteristics of a side-lobe or an artifact; however, they are located in a noisy region or close to a very bright source. Finally, we identified 701 as *real sources*, and included all detections with a S/N ratio ≥ 5 that are not elongated (and thus a not part of sidelobes). Table 5 summarizes the numbers of detected sources ascribed to the different categories.

4. Final Catalog

After removing all artifacts extracted by `BLOBCAT`, the final catalog consists of 11 211 entries. From these, 9 254 represent discrete sources; the remaining are part of LSS and SNR candidates.

Table 4. Statistics of the matches between GLOSTAR D-configuration and other published surveys. A match radius of 10″ and 6″ has been used, centered on the peak of the GLOSTAR emission.

Survey	Ref.	Wavelength	Resolution (″)	rms level mJy beam^{-1}	Num. of sources in GLOSTAR region	Num. of matches (10″)	Num. of matches (6″)
THOR	(1)	20 cm	25	0.3-1	6 337	5 179	5 092
RMS	(2)	6 cm	1.0-2.0	0.22	737	150	145
CORNISH	(3)	6 cm	1.5	0.33	1 754	1 231	1 221
GLOSTAR B configuration	(4)	6 cm	1.0	0.08	5 437	2 496	2 473
ATLASGAL	(5)	870 μm	19.2	50-70	3 096	198	109
HiGAL	(6)	70-500 μm	5.8-35	$\cdots$	35 344	1 096	918
WISE	(7)	3.4-22 μm	6-12	$\cdots$	2 426 781	5 473	3 034
GLIMPSE	(8,9)	3.6-8.0 μm	1.4-2	$\cdots$	18 100 849	7 326	5 525

References are: (1) Wang et al. (2018), (2) Urquhart et al. (2009), (3) Hoare et al. (2012), (4) Yang et al. (2023), (5) Schuller et al. (2009), (6) Molinari et al. (2016), (7) Wright et al. (2010), (8) Churchwell et al. (2009) and (9) (Fazio et al. 2004).

Table 5. Summary of detection categories.

Description	Number of sources
Total number of extracted sources	13 001
Number of sources assoc. with large structures	839
Number of sources assoc. with SNR	1 126
Number of sources with a counterpart	8 235
Number of sources with $Y_{factor} > 3$	297
Number of recovered real sources	701
Number of unclear sources	19
Number of artifacts or side lobes[a]	1 790
Number of sources in final catalog	11 211

[a] Excluded from final catalog.

In this section, we will use the discrete sources and compare them with previous surveys in order to quantify the reliability of their properties based on our source extraction process (see Sect. 3.2). Additionally, we use the information from the counterparts of previous radio and infrared surveys to classify the sources.

4.1. Astrometry

To check the quality of the GLOSTAR source positions, we have compared the positions of unresolved ($Y_{factor} < 1.2$) sources that have counterparts in the radio fundamental catalog of compact radio sources[7]. These radio sources are quasars that were observed with Very Long Baseline Interferometry (VLBI) and their celestial positions are known with accuracies better than a few milli-arcseconds.

Using a position matching of 6″ between both catalogs, we found 55 sources in common. In the upper panel of Fig. 6, we show the ℓ and b position offsets between GLOSTAR D-configuration and VLBI sources. The mean values of the position offsets are $-0.''34\pm0.''10$[8] and $+0.''31\pm0.''11$ in Galactic longitude and latitude, respectively. The standard deviations of the offsets are $0.''8$ in both directions. Thus, the positions of the GLOSTAR catalog presented in this paper are accurate to within 1″.

A second test can be done by comparing the GLOSTAR sources with the CO-Ordinate Radio 'N' Infrared Survey for

High-mass star formation (CORNISH; Purcell et al. 2013) catalog. CORNISH used the VLA prior to its upgrade to observe at 5.0 GHz an area similar to that covered by us. Most of the sources in this catalog are expected to be background extragalactic objects, which is also the case observed for GLOSTAR. No detectable proper motions are expected from these sources. We have also used a matching radius of 6″, and we have restricted our analysis to sources that are unresolved in both catalogs. In the lower panel of Fig. 6, the measured position offsets of 668 sources meeting these criteria are shown. The mean values of the position offsets are $-0.''30\pm0.''04$ and $+0.''28\pm0.''04$ in ℓ and b, respectively. The standard deviation of the offsets is $0.''80$ in both Galactic coordinates. This result is in agreement with that found for the VLBI sources.

4.2. Flux density levels

In this section, we will check the accuracy of flux density measurements. By using the 668 CORNISH unresolved sources detected in the GLOSTAR survey, we can check the quality of the measured flux densities in GLOSTAR (Medina et al. 2019; Dzib et al. 2023; Yang et al. 2023). This can be done since most of these sources are background extragalactic objects whose radio emission is expected to have a low degree of variability.

In the upper panel of Fig. 7, the flux densities of the CORNISH sources are plotted against the GLOSTAR flux densities. For a visual guide, the equality line is also shown. This panel shows that the radio emission from both catalogs is consistent. In the lower panel of Fig. 7, the distribution of the ratios of the flux densities of sources from both catalogs are shown, with mean and standard deviation values of 1.01 ± 0.02 and 0.42, respectively. Taking a 3σ value, it is then concluded that the fluxes of the GLOSTAR survey have an accuracy better than 6%.

4.3. Source effective radius

The BLOBCAT software returns the number of pixels within a source (output parameter *npix*). This number does not contain any information on the structure, elongation, or position angle of the source. While source size cannot be recovered from BLOBCAT, following the strategy by Medina et al. (2019) we can determine the effective radius of a source.

We aim to estimate the radius of a circular source that covers the same number of pixels as the source extracted using BLOBCAT. The area of a single pixel in the GLOSTAR D-configuration images is $2.''5 \times 2.''5$. The area, A, covered by a

---

[7] This catalog is provided via the project webpage at `https://astrogeo.smce.nasa.gov`. Responsible NASA official: L. Petrov.

[8] The errors reported on the mean values, here and through the manuscript, are estimated using the standard error of means (SEM = $\sigma/\sqrt{N}$, where σ is the standard deviation and N is the number of elements in the sample).
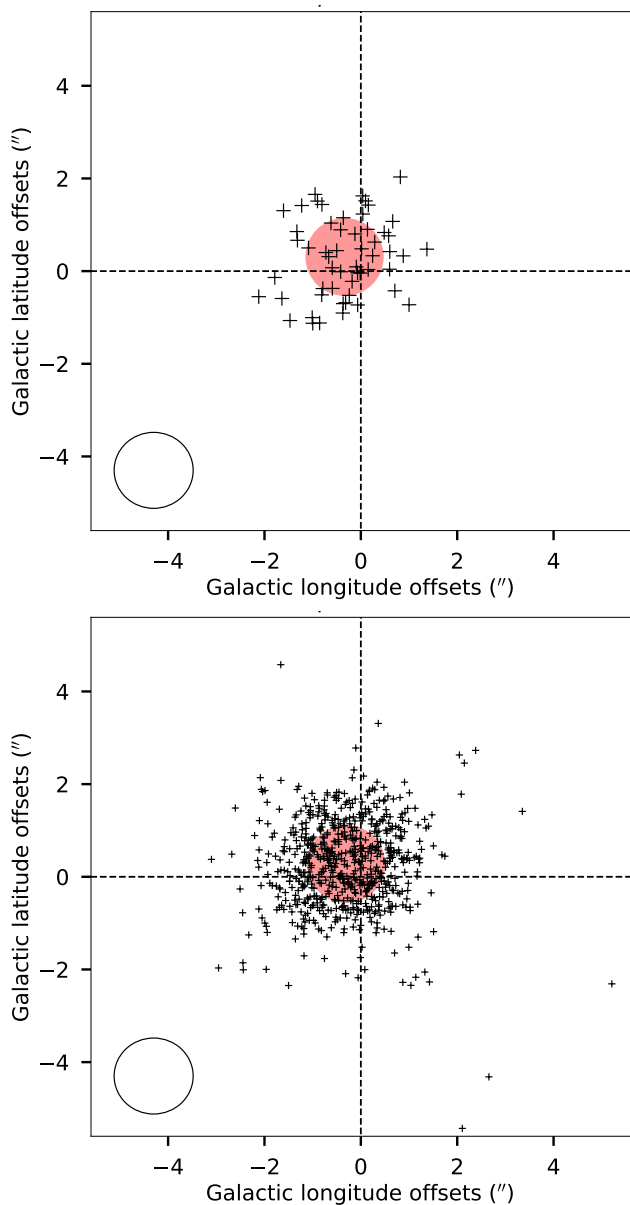
Fig. 6. Position offsets between GLOSTAR unresolved sources (Y factor ≤ 1.2) and VLBI extragalactic sources (upper panel), and CORNISH unresolved sources (lower panel). Red circles are centered in the mean values of the offsets, and the radii sizes are equal to the standard deviations. The circles in the bottom left corners of both panels represent the mean position error of GLOSTAR-VLA D-configuration radio sources reported in this work, which is 1.″6.

Fig. 7. *Upper panel:* Comparison of the flux densities of CORNISH unresolved sources that are also detected as unresolved sources in the GLOSTAR survey (this work). The black dashed line is the line of equality. *Lower panel:* Flux density ratio distribution of sources plotted in the upper panel. The mean value of the flux density ratios is 1.01 ± 0.02 and the standard deviation is 0.42.

source is `npix` times the pixel size squared, and the effective source radius is given by

$$R_{\text{source}} = \sqrt{\frac{A}{\pi}}.$$

The effective radius, as obtained from this procedure, is listed for all sources in Table 7.

4.4. Spectral indices

The flux density of radio sources as a function of the observed frequency can expressed in a power law form:

$$S_\nu \propto \nu^\alpha, \tag{3}$$

where S_ν is the flux density at the observed frequency, ν, and α is the spectral index. The sensitive and wideband GLOSTAR-VLA observations allow determining an in-band spectral index (α_{GLOSTAR}). We will follow the successful strategy used in the other GLOSTAR-VLA catalogs (Medina et al. 2019; Dzib et al. 2023; Yang et al. 2023). First, to avoid possible spectral index biases, we constrain our spectral index determinations to sources with S/N ratio > 10 and $Y_{\text{factor}} \leq 2.0$, that is, compact sources. A lower limit for the S/N ratio was chosen to ensure that the source could be detected in most of the seven frequency bin images. For instance, as the noise level per frequency bin image is expected to be $\sqrt{7}\times$ larger than that of the combined image, for sources with S/N=10 we expect detection of the order of $10/\sqrt{7} = 3.8\sigma_{\text{bin}}$ in each frequency bin image. This rough value ensures detections in most frequency bin images. For extended

sources, as the (u, v)-coverage is different across the band, the fraction of total flux density recovered at the lower sideband can greatly exceed that at the upper sideband. In these cases, the spectral index derived will have apparently steeper (more negative) spectra to values that can be physically impossible. Second, source flux densities are measured on the imaged frequency bins (see Sect. 2). We use the logarithmic form of Equation 3, which is a linear equation, and the measured flux densities in the individual frequency bin images to perform a least-squares fitting and determine the spectral index. Following these steps, we have estimated the spectral indices of 3 968 sources.

In Dzib et al. (2023) and Yang et al. (2023), we have compared the spectral indices determined from GLOSTAR data with those determined by the THOR survey (Wang et al. 2018) for compact common sources. We have found a good consistency between the spectral index determination by both surveys. The THOR survey covered the full L-band (1.0–2.0 GHz) with the VLA, and they also split their observed bandwidth into smaller frequency chunks to estimate the in-band spectral index (see Wang et al. 2020, for details). Though THOR observed at lower frequencies frequency than GLOSTAR, the resulting angular resolution of their images is similar to that of the GLOSTAR-VLA D-configuration images (18″ for GLOSTAR and 25″ for THOR). Thus, following Medina et al. (2019), we now proceed to determine the source spectral indices from the peak flux densities measured by GLOSTAR and THOR ($\alpha_{\mathrm{GLOSTAR-THOR}}$). We consider mid-frequencies of 1.5 GHz and 5.8 GHz for THOR and GLOSTAR, respectively. As only two flux density values are considered, the spectral index can be determined as

$$\alpha_{\mathrm{GLOSTAR-THOR}} = \frac{\ln\left(S_{\mathrm{GLOSTAR}}/S_{\mathrm{THOR}}\right)}{\ln(5.8/1.5)},$$

where S_{THOR} and S_{GLOSTAR} are the peak flux densities from the respective survey. The spectral index uncertainty is calculated using:

$$\sigma_{\alpha_{\mathrm{GLOSTAR-THOR}}} = \frac{\sqrt{(\sigma_{S_{\mathrm{THOR}}}/S_{\mathrm{THOR}})^2 + (\sigma_{S_{\mathrm{GLOSTAR}}}/S_{\mathrm{GLOSTAR}})^2}}{\ln(5.8/1.5)},$$

which is obtained following standard error propagation theory. $\sigma_{S_{\mathrm{GLOSTAR}}}$ and $\sigma_{S_{\mathrm{THOR}}}$ are the source flux density uncertainties for GLOSTAR and THOR. In the case of the THOR survey, their catalog does not contain direct values for flux density uncertainties. However, since their S/N ratio is given, the THOR flux density uncertainty can be estimated as

$$\sigma_{S_{\mathrm{THOR}}} = \frac{S_{\mathrm{THOR}}}{\mathrm{S/N}}.$$

With this procedure, we estimate $\alpha_{\mathrm{GLOSTAR-THOR}}$ for 4 127 radio sources, of which 1 308 do not have an estimated value of $\alpha_{\mathrm{GLOSTAR}}$.

The total number of radio sources with an estimated radio spectral index, either the GLOSTAR-inband or GLOSTAR-THOR, is 5 276. Results of both $\alpha_{\mathrm{GLOSTAR}}$ and $\alpha_{\mathrm{GLOSTAR-THOR}}$ on individual sources are listed in Table 7 and they will be compared in Sect. 5.3.

4.5. Counterparts in other surveys

During the last few decades, Galactic Plane surveys have addressed many aspects of high-mass star ($> 8\,M_{\odot}$) formation. As these surveys image large areas of the Galaxy, they provide unbiased samples of star-forming regions with different properties (see, for example Urquhart et al. 2018, 2022; Elia et al. 2017).

As we have seen in previous sections, information from other radio surveys, such as CORNISH and THOR, can corroborate and complement the source parameters from our catalog. Additionally, information at shorter wavelengths can be used to give insights into the nature of the observed radio sources. In the context of GLOSTAR, particularly interesting radio sources are those related to star formation. CORNISH and THOR were briefly described in previous sections and in the following we describe the other Galactic plane surveys used to characterize the GLOSTAR radio sources.

Recently, we have presented the *GLOSTAR VLA B-configuration catalog* of the Galactic plane using higher angular resolution (1″) images (Yang et al. 2023). The imaged field covers the area $|b| \leq 1.0°$, and the Galactic longitude ranges $2° < \ell < 40°$ and $56° < \ell < 60°$; i.e., 32 square degrees less than the GLOSTAR VLA D-configuration. About 5 500 radio sources were reported and classified. Using a crossmatch radius of 10″, we found a match for 2 497 compact radio sources.

The *Red MSX Source* (RMS) survey was a multi-wavelength project aiming to identify massive young stellar objects (MYSO) in the Galactic plane (Hoare et al. 2005; Lumsden et al. 2013). Using a multi-wavelength classification scheme, RMS identifies the nature of radio sources; particularly within the northern hemisphere they identified 79 PNe and 391 H ɪɪ regions with radio emission (Urquhart et al. 2009). We retrieved 150 of the RMS sources within a search radius of 10″.

Emission at sub-millimeter wavelengths is dominated by dense cool dust and gas, which is intimately related to star formation. At these wavelengths, the *APEX Telescope Large Area Survey of the Galaxy* (ATLASGAL; Schuller et al. 2009) is the first high-resolution ($\approx 20″$ FWHM) ground-based submillimeter ($870\,\mu\mathrm{m}$) survey of the thermal dust emission in the entire inner Galactic plane. The ATLASGAL survey has presented $> 10\,000$ dense clumps in the Galactic plane (Contreras et al. 2013; Csengeri et al. 2014; Urquhart et al. 2014). Correlating radio sources (such as those detected in GLOSTAR) with ATLASGAL clumps is an excellent way to identify embedded or dust-enshrouded objects such as UC-H ɪɪ regions (see, for example, Medina et al. 2019; Irabor et al. 2018; Urquhart et al. 2007, 2009, 2013; Purcell et al. 2013). Correlating our radio source catalog with the ATLASGAL compact source catalog (Urquhart et al. 2014), we find cross match 281 sources within 10″.

The *Herschel Infrared Galactic plane survey* (HiGAL) is a photometric survey in five far-infrared (FIR) bands between 70 and $500\,\mu\mathrm{m}$ (Molinari et al. 2016). Its observations covered the whole Galactic plane with a varying latitude range (Elia et al. 2021). The FWHM beam sizes range from 6″ to 35″, and the mean position uncertainty is 1.″2 (Molinari et al. 2016). Using a cross matching radius of 10″ we found 1527 sources in both our GLOSTAR and the HiGAL catalogs.

The Wide-field Infrared Survey Explorer (WISE) was a NASA infrared-wavelength astronomical space telescope mission (Wright et al. 2010) that mapped the entire sky in four midinfrared (MIR) bands W1, W2, W3, and W4 centered at 3.4, 4.6, 12, and $22\,\mu\mathrm{m}$, respectively, using a 40 cm telescope feeding an array with a total of 4 million pixels; these wavelengths correspond to angular resolutions of 6.″1, 6.″4, 6.″5, and 12″. The WISE All-sky release source catalog contains the source properties of ~ 563 million sources. The WISE All-sky release source catalog has been filtered out for sources with S/N< 5, spurious

detections, and image artifacts[9]. Using a radius of 10″ for cross matching GLOSTAR radio sources and sources from the WISE All-sky release source catalog, we found 7 298 common sources. However, as mentioned earlier, because of the high density of WISE detected sources, mostly foreground field stars, there is a significant probability of false matches and we have reduced the cross matching criteria to 6″ and found 3 034 matching sources.

Finally, we have also used the point source catalog[10] from the Galactic Legacy Infrared Mid-Plane Survey Extraordinaire (GLIMPSE; Churchwell et al. 2009). This legacy project was conducted with the Spitzer space telescope and observed the shorter wavelength part of the MIR range; that is, at 3.6, 4.5, 5.8, 8.0 μm. GLIMPSE is composed of several surveys, and particularly interesting for GLOSTAR are GLIMPSEI and GLIMPSEII which, combined, effectively observed the Galactic plane from $-70° < \ell < 65°$ and $|b| < 1°$. Using a cross matching criterion of 10″, we found 7 326 GLIMPSE counterparts to radio sources. However, similar to the WISE catalog, a large number of these are expected to be foreground objects. Thus, we reduced the cross match radius to 6″ for the final counterpart search and found 5 525 counterparts.

4.6. Source classification

The present catalog is composed of 11 211 radio sources, and thus one-by-one source classification, as performed in our previous work (i.e., Medina et al. 2019), is a time-consuming task. Furthermore, in our previous catalog work, we have shown that the classification of radio sources detected within the GLOSTAR-VLA project is largely (> 90%) compatible with the classifications made by other radio surveys (Medina et al. 2019; Dzib et al. 2023; Yang et al. 2023). Notably, in the GLOSTAR-VLA pilot region, the source classifications in the high-resolution and low-resolution maps are also highly consistent (Dzib et al. 2023). Thus, our source classification approach for the present catalog is slightly different and is presented below. We focus the source classification analysis on the 9 227 sources that are not related to LSSs (839 sources) or SNRs (1 126 sources) or Unclear (19).

4.6.1. Source classification from other surveys

First, we identify sources with counterparts in other catalogs and use their classification. We prioritize the catalogs in the following order: GLOSTAR-VLA B-configuration (Yang et al. 2023), CORNISH (Purcell et al. 2013), RMS (Urquhart et al. 2009), WISE H ɪɪ regions (Anderson et al. 2014), and THOR (Wang et al. 2020). We also check the GLOSTAR-VLA 6.7 GHz methanol maser catalog (Nguyen et al. 2022), as this maser line is only detected toward MYSOs.

The above catalogs use different names for different classes of sources. To homogenize them, we have used the classifications chosen in previous GLOSTAR-VLA catalogs. These classifications are *HII* for H ɪɪ regions and H ɪɪ region candidates, *PN* for planetary nebulae and planetary nebula candidates, *EgC*

for background extragalactic candidate sources, *Psr* for pulsars, *Radio-star* for stars with radio emission, and *other* for sources that could not be classified within our classification scheme. The CORNISH survey used the terms UCHII and HII-Region, which, in our final classification, are renamed as HII. Sources CORNISH classified as Radio Galaxy (Central Source), Radio Galaxy (lobe), Galaxy, and IR-Quiet are renamed as EgC. Sources classified as H ɪɪ region and HII/YSO in the RMS survey are categorized as HII, while YSO and Evolved star classifications are renamed as Radio-star in our catalog. Regardless of the H ɪɪ region sub-classification from (Anderson et al. 2017), we rename these sources as HII. From the THOR survey, we discarded the classification X-ray (which only accounts for a counterpart at another wavelength) and renamed their *jet* classification to EgC (see also Wang et al. 2018). Sources associated with methanol masers are labeled as HII, as they represent objects in the very early phases of high-mass star formation. While most class II methanol masers are not associated with compact radio emission, some of them are: in the GLOSTAR D array data, Nguyen et al. (2022) find that toward 12% of the 554 detected methanol masers also radio continuum is detected (while 97% are associated with dust emission.

The number of classified radio sources from other surveys is 3 302. The numbers of adopted classifications are 2 286 from GLOSTAR-VLA B-configuration, 537 from CORNISH, 57 from RMS, 167 from WISE H ɪɪ regions, 249 from THOR, and six sources from the 6.7 GHz methanol maser catalog. Classifications and references to the classification origins are given in Table 7. We note that a large fraction of GLOSTAR radio sources could not be classified by only using the information from other surveys.

4.6.2. Source classification from information at shorter wavelengths

After the cross match classification, there are still 5 925 unclassified sources. To classify them, we use the information obtained in surveys conducted at other than radio wavelengths. We follow similar criteria as used in the previous GLOSTAR-VLA catalogs.
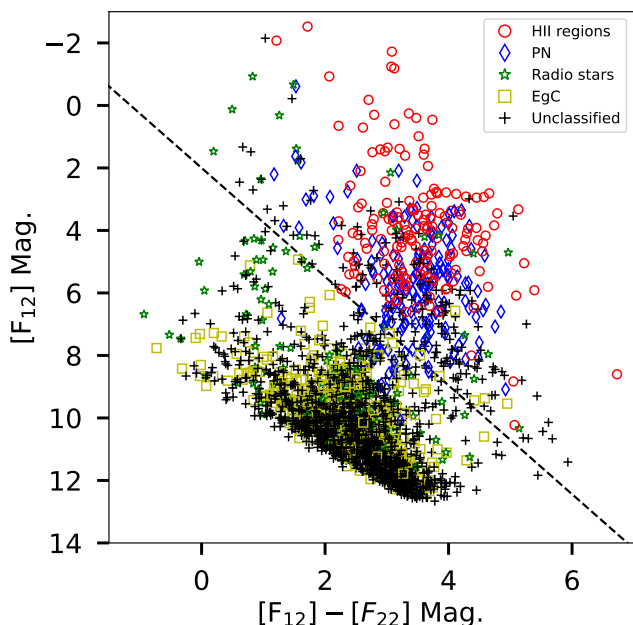
First, compact ($Y_{factor} \leq 2.0$) radio sources that do not have counterparts at submm, FIR, and MIR wavelengths are likely to be background extragalactic sources (Hoare et al. 2012; Lucas et al. 2008; Marleau et al. 2008; Medina et al. 2019), and thus they are classified as EgC. By matching these criteria, we classified 1 569 radio sources as EgC.

The *HII* region candidate classification is assigned to radio sources that have a counterpart at submm wavelengths or that have a counterpart only at FIR wavelengths (Hoare et al. 2012; Anderson et al. 2012; Urquhart et al. 2013; Yang et al. 2021). There are 32 radio sources with counterparts in the ATLASGAL submm survey, and 82 sources with a counterpart only in the HiGAL FIR survey. All of these 114 sources are classified as H ɪɪ region candidates.

If radio sources have counterparts only at FIR and MIR wavelengths, additional criteria are needed to classify them. Extended sources can, for example, represent photo dissociated regions (PDRs), parts of SNRs, or parts of extended H ɪɪ regions and complicate the classification procedure. While these may include interesting cases, for the purpose of this paper we concentrate on compact radio sources with the signatures of early phases of star formation. Thus, in the following, we will focus on the classification of compact radio sources ($Y_{factor} \leq 2.0$). The

---

[9] Detailed information on WISE data processing and source catalogs (including rejected detections) can be found in `https://wise2.ipac.caltech.edu/docs/release/allsky/`.

[10] The GLIMPSE point Source Catalog (GLMC) is the most reliable of GLIMPSE catalogs with a reliability ≥ 95% (Churchwell et al. 2009). The GLMC can be found at the following sites: `http://ssc.spitzer.caltech.edu/legacy/glimpsehistory.html` and `http://irsa.ipac.caltech.edu/data/SPITZER/GLIMPSE`.

Fig. 8. Mid-infrared color-magnitude diagram of GLOSTAR radio sources with a WISE counterpart. The dashed line indicates the constraint used by Medina et al. (2019) to distinguish between different types of objects.

1 463 sources with $Y_{factor} > 2.0$ that have not been previously classified, are classified as *Unclassified* in our final catalog.

The 2 779 remaining unclassified compact radio sources have counterparts at FIR or MIR wavelengths. Medina et al. (2019) constructed [12] vs. [12]–[22] color-magnitude diagram using mid IR magnitudes from the WISE catalog and showed that in the resulting diagram the H II regions and PNe occupy a different area than radio stars and other unclassified objects (which have more likely an extragalactic origin, see discussion by Medina et al. 2019). As discussed by Medina et al. (2019), H II regions and PNe fulfill the constraint (hereafter the color-magnitude constraint):

$$[12]Mag. < 1.74 \times ([12] - [22]) + 2,$$

while Radio-stars and EgC do not.

To illustrate the situation for the GLOSTAR radio sources discussed in this work, we use the flux information from WISE. A total of 2 401 GLOSTAR radio sources have counterparts detected in the 12 and 22 μm WISE bands. These include 178 H II regions, 175 PNe, 452 EgC, 159 radio-stars, and 1 437 unclassified sources. In Fig. 8, we plot the color-magnitude diagram [12] vs. [12]–[22] of these sources, where the source types are distinguished with different markers and colors. The line that follows the color-magnitude constraint is also plotted as a dashed line. Fig. 8 clearly shows that H II regions and PNe occupy different areas in this diagram than the radio stars and EgC objects.

From the already classified sources, we notice that 360 lie above the color-magnitude constraint line, and these are divided into 178 (50%) H II regions, 152 (42%) PNe, 7 (2%) EgC, and 23 (6%) radio stars. Thus, we can assume that sources that fall above the color-magnitude constraint are either H II regions or PNe. There are 153 unclassified sources fulfilling these criteria, and in this work we classify them as H II region candidates, labeled as HII in the signal catalog; we notice that up to 50% will likely be PNe; however, given the current analysis, it is not possible to definitively characterize them.

On the other hand, 604 classified sources do not comply with the color-magnitude constraint and these are divided into 23 (4%) PNe, 445 (74%) EgC, and 136 (22%) radio stars. We notice that EgC sources constitute the majority in this region of the color-magnitude diagram. Following these counts, we classify the 1 284 previously unclassified sources in this area as EgC, noting that about 25% of them may likely be galactic sources; however, it is not possible to differentiate them with the current data.

The IR information of the remaining sources is scarcer than for the previous cases, and MIR colors cannot be obtained as fluxes are only reported in a single band. We noticed that 86 of these sources have at least a counterpart in one of the FIR bands. As FIR emission may trace cold dust, radio sources associated with FIR emission might be related to H II regions, and accordingly we classify them as H II region candidates (labeled as HII in the final catalog). However, further studies are required to confirm the nature of these sources. The 1 256 remaining sources have counterparts only in the MIR range. These can be either EgC or radio stars, however our previous work (Medina et al. 2019; Dzib et al. 2023; Yang et al. 2023) has shown that most sources with only MIR and near-infrared counterparts are background extragalactic sources. Accordingly, these 1256 sources are classified as EgC. A summary of the classified sources per method is given in Table 6. Class and classification methods are given in the catalog and Table 7.

Table 6. Summary of classification categories.

Class	Method	Number of sources
HII	Other catalog	410
	Methanol maser	6
	SMM counterpart	32
	Only FIR counterpart	82
	Color-magnitude constrain	153
	FIR counterpart, no color with MIR	86
	Total	769
PNe	Previously known source	240
Radio-star	Previously known source	425
PSR	Previously known source	6
PDR	Previously known source	1
EgC	Previously known source	2203
	No SMM or IR counterpart	1569
	Color-magnitude constrain	1284
	Only MIR counterparts	1256
	Total	6312
Other	Previously known source	19
	$Y_{factor} > 2$ & no previous class	1463
	Total	1482

Table 7. GLOSTAR source catalog for the region.

GLOSTAR name	ℓ	b	S/N	S_{peak}	$\sigma_{S_{peak}}$	S_{int}	$\sigma_{S_{int}}$	Y_{factor}	Radius	\multicolumn{4}{Spectral index}				\multicolumn{5}{Radio}					submm	\multicolumn{3}{IR}			Class	Ref.	Method
	(°)	(°)		(mJy beam⁻¹)		(mJy)			('')	α	$\Delta\alpha$	α^*	$\Delta\alpha^*$	GB	C	R	T	MM	A	H	W	G			
(1)	(2)	(3)	(4)	(5)	(6)	(7)	(8)	(9)	(10)	(11)	(12)	(13)	(14)	(15)	(16)	(17)	(18)	(19)	(20)	(21)	(22)	(23)	(24)	(25)	(26)
G002.005+00.348	02.0047	+0.3479	09.2	1.29	0.16	1.34	0.16	1.0	13.10	...	...	...	...										EgC	1	No SMM or IR counterpart
G002.007–00.681	02.0072	-0.6806	170.3	26.07	1.41	121.27	6.07	4.7	52.00	...	...	...	...							Y			HII	1	Only FIR counterpart
G002.011+00.108	02.0111	+0.1076	05.4	0.75	0.14	1.10	0.15	1.5	12.50	...	...	...	...							Y			EgC	1	No SMM or IR counterpart
G002.012+00.744	02.0120	+0.7438	178.3	15.20	0.82	13.67	0.69	0.9	21.10	...	...	-0.16	0.05	Y						Y	Y		PN	2	Previously known source
G002.013+00.896	02.0125	+0.8959	05.3	0.46	0.09	0.57	0.09	1.2	11.10	...	...	...	...								Y		EgC	1	Color-magnitude constrain
G002.018+00.669	02.0177	+0.6688	32.2	3.12	0.19	3.52	0.20	1.1	20.20	...	...	-0.33	0.25	Y							Y		Other	2	Previously known source
G002.021–00.824	02.0210	-0.8243	19.0	1.92	0.14	1.65	0.13	0.9	14.40	...	...	0.07	0.18							Y	Y		HII	1	Color-magnitude constrain
.	.	.	.	.	.	.	.	.	.	.	.	.	.	.	.	.	.	.	.	.	.	.	.	.	.
G021.103–00.976	21.1032	-0.9757	15.3	2.89	0.24	2.67	0.23	0.9	14.20	0.26	0.15	0.04	0.24	Y		Y						Y	Radio-star	2	Previously known source
G021.103+00.664	21.1034	+0.6639	07.4	0.60	0.09	0.51	0.09	0.8	10.60	...	...	...	...			Y					Y	Y	EgC	2	Previously known source
G021.114+00.872	21.1137	+0.8723	05.1	0.43	0.09	0.44	0.09	1.0	9.70	-0.96	0.20	...	...	Y			Y				Y	Y	Radio-star	2	Previously known source
G021.121–00.956	21.1206	-0.9563	05.6	0.91	0.17	1.29	0.17	1.4	12.10	...	...	...	...	Y								Y	EgC	2	Previously known source
G021.126–00.294	21.1258	-0.2944	17.2	5.42	0.43	204.65	10.24	37.7	106.60	0.11	0.12	...	...				Y						LSS	1	Visual Inspection
G021.130–00.247	21.1300	-0.2465	05.4	1.63	0.31	17.96	0.95	11.0	31.80	...	...	...	...										LSS	1	Visual Inspection
G021.145+00.585	21.1445	+0.5854	05.9	0.49	0.09	0.68	0.09	1.4	12.60	...	...	...	...										EgC	1	No SMM or IR counterpart
.	.	.	.	.	.	.	.	.	.	.	.	.	.	.	.	.	.	.	.	.	.	.	.	.	.
G047.145–00.166	47.1451	-0.1660	04.1	0.25	0.06	0.23	0.06	0.9	7.70	...	...	...	...									Y	EgC	1	Only MIR counterparts
G047.147+00.730	47.1471	+0.7299	20.1	1.36	0.10	11.02	0.56	8.1	46.90	...	...	...	...										SNR	7	Previously known SNR
G047.147–00.113	47.1472	-0.1132	05.1	0.31	0.06	0.28	0.06	0.9	9.00	...	...	...	...									Y	EgC	1	Only MIR counterparts
G047.154+00.890	47.1540	+0.8903	24.6	1.52	0.10	1.72	0.11	1.1	18.90	-0.22	0.07	-0.64	0.30				Y					Y	EgC	1	Only MIR counterparts
G047.162–00.513	47.1617	-0.5132	04.5	0.28	0.06	0.21	0.06	0.8	7.50	-0.55	0.22	...	...				Y						EgC	1	No SMM or IR counterpart
G047.171–00.621	47.1708	-0.6208	04.0	0.24	0.06	0.16	0.06	0.6	6.30	...	...	...	...								Y	Y	EgC	1	Color-magnitude constrain
G047.172–00.481	47.1722	-0.4806	08.5	0.52	0.07	0.39	0.06	0.8	10.60	-0.52	0.13	...	...				Y					Y	EgC	1	Only MIR counterparts
.	.	.	.	.	.	.	.	.	.	.	.	.	.	.	.	.	.	.	.	.	.	.	.	.	.
G059.932+00.837	59.9320	+0.8368	55.7	5.88	0.33	7.02	0.37	1.2	21.60	-0.47	0.04	-0.66	0.11				Y						EgC	1	No SMM or IR counterpart
G059.937–00.353	59.9365	-0.3528	05.2	0.88	0.18	0.93	0.18	1.1	10.00	-0.43	0.16	...	...				Y				Y	Y	SNR	7	Previously known SNR
G059.940–00.157	59.9399	-0.1569	39.4	6.92	0.41	7.06	0.39	1.0	18.60	-0.03	0.05	0.36	0.12		Y		Y						EgC	3	Previously known source
G059.941–00.042	59.9413	-0.0417	28.6	4.86	0.31	5.58	0.33	1.1	18.80	-0.52	...	-0.88	0.23				Y						EgC	1	No SMM or IR counterpart
G059.948+00.555	59.9478	+0.5549	14.6	1.83	0.16	1.67	0.15	0.9	14.00	-0.13	0.09	-0.28	0.28				Y				Y	Y	EgC	1	Color-magnitude constrain
G059.963+00.036	59.9629	+0.0361	04.6	0.94	0.21	1.26	0.21	1.3	10.20	...	...	...	...								Y	Y	EgC	1	Color-magnitude constrain
G059.968+00.660	59.9680	+0.6597	07.1	1.17	0.18	0.89	0.17	0.8	11.00	-0.04	0.14	...	...				Y				Y	Y	EgC	1	Color-magnitude constrain

Notes: The columns are, from left to right, the source name, Galactic coordinates, the signal-to-noise ratio, the peak and integrated flux densities and their errors, the Y-factor, the effective radius, the estimated spectral indices determined from the GLOSTAR and THOR flux densities and from only the in-band GLOSTAR sub-images (*). Columns 15 to 23 list if the source has a counterpart in other surveys. Radio: GB for GLOSTAR B-configuration catalog (Yang et al. 2023), C for CORNISH (Hoare et al. 2012; Purcell et al. 2013), R for RMS (Urquhart et al. 2009), T for THOR (Beuther et al. 2016; Wang et al. 2020), and MM for methanol masers surveys (Nguyen et al. 2022; Green et al. 2009). Submillimeter/FIR: A for ATLASGAL (Urquhart et al. 2018). Infrared: H for HiGAL (Molinari et al. 2016), W for WISE (Wright et al. 2010), and G for GLIMPSE (Churchwell et al. 2009). Column 24 lists the final classification of the radio sources. References in column 25 are as follows: (1) This work, (2) Yang et al. (2023), (3) Purcell et al. (2013), (4) Urquhart et al. (2009), (5) Anderson et al. (2014), (6) Wang et al. (2020), (7) SNR remnants catalogs by Dokara et al. (2021) or Green (2019), and (8) Methanol maser catalogs by Nguyen et al. (2022) or Green et al. (2009). Finally, column 27 lists the method used for the source classification.
Only a small portion of the data is provided here, and the full table is available in electronic form at the CDS via anonymous ftp to cdsarc.u-strasbg.fr (130.79.125.5) or via http://cdsweb.u-strasbg.fr/cgi-bin/qcat?J/A&A/ and through the dedicated GLOSTAR webpage at https://glostar.mpifr-bonn.mpg.de/glostar/.

5. Summary of full catalog

The final catalog consists of 11 211 entries, 1 965 of which are related to extended structures (for example, SNRs or extended H II regions) and 19 are sources of uncertain nature that could not be identified as real or spurious sources. Source classification was possible for most of the remaining sources, but 1468 extended sources ($Y_{factor} > 2$) were classified as *Unclassified* as their extended structures require a deeper analysis to classify them, which goes beyond the scope of the present work. In the following, we will discuss the remaining classified sources. This discussion will focus on the spatial distribution, flux densities, sizes, and spectral indices of the sources. Also, we will discuss the identified H II region candidates.

5.1. Spatial distribution

The Galactic disk hosts most of its star-forming regions in its inner parts. Basic source properties, namely intensity and angular size, depend on their distance, which is determined by their location in the Galaxy.
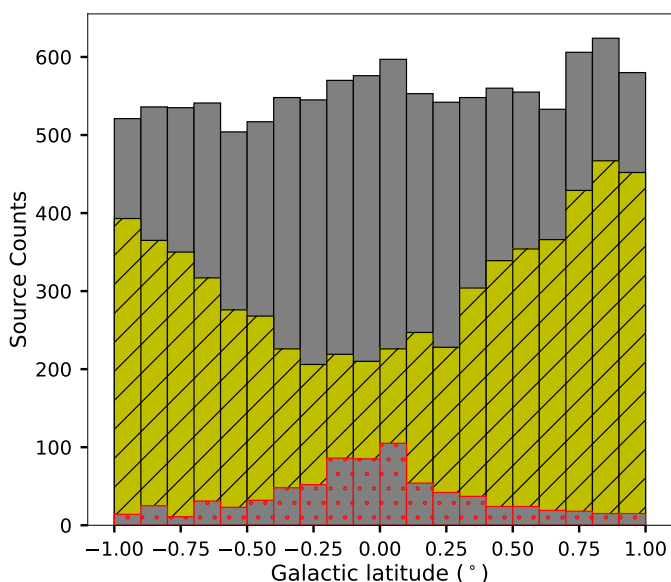
Fig. 9. Source distribution of GLOSTAR D-configuration sources in the Galactic latitude. Color bars are: full sample in gray, yellow for EgC sources and red for H II regions. The bin size is 0.1°.

Figures 9 and 10 show the distribution of all detected GLOSTAR sources. The overall distribution in the observed Galactic latitude range is robustly uniform (Fig. 9). When we only consider the EgC sources (yellow bars), it can be noticed that their number diminishes towards the Galactic mid-plane ($b = 0°$). Moreover, as can be seen from Fig. 1, most of the extended sources are found around this latitude line, and it is also where most of the star formation is expected. The extended structures have two effects on source identification: they confuse background sources and, in interferometric images with no zero-spacing information, they also increase the noise levels. Thus, background extragalactic sources that are intrinsically uniformly distributed in the sky show a decreasing number towards the mid-plane. On the contrary, H II regions (red bars) are more numerous towards low Galactic latitudes; that is, where most of the star formation in the Galaxy is occurring.

The source distribution in Galactic longitude, Fig. 10, also looks uniform for $\ell < 56°$, with the source counts increasing at larger longitudes. The area with $\ell > 56°$ contains a small number of LSSs, resulting in an improvement of the noise level (see also Table 2) and less compromised sources. As a consequence, a higher number of sources are detected at these longitudes. However, the number of H II regions in this area is also lower, indicating a lower number of star-forming sites. This is in concordance with the dearth of MYSOs that Zhang et al. (2019) noted in the segment of the Perseus arm stretching between $\ell = \sim 50°$ and 90°.

Finally, in Fig. 11, we show the complete spatial distribution of radio sources detected in the course of this work. We have included the sources with LSS and SNRs. This figure shows that the number of sources is lower in the presence of extended sources because of the effects mentioned earlier.

5.2. Fluxes and angular sizes

The source flux density is one of the most critical parameters in the GLOSTAR source catalog. By comparing our results with the CORNISH survey, we have shown that the flux density parameter from the GLOSTAR survey is accurate within 6% (see Section 4.2). The CORNISH survey, however, had a nominal noise level of ~0.4 mJy beam^{-1}, significantly higher than the GLOSTAR D-configuration images. In the top panel of Fig. 12, we show the source peak flux density distribution for GLOSTAR and CORNISH for the Galactic plane area covered by this work. The better sensitivity of the GLOSTAR survey resulted in a larger number of detected sources, indicating that most sources with a brightness lower than a few mJy beam^{-1} are new detections.

The ratio S_{int}/S_{peak} is also known as the Y-factor, a parameter that can be used to infer the size of a source. In the GLOSTAR survey, we have used it to define an unresolved source when the $Y_{factor} \leq 1.2$, a compact source when $1.2 < Y_{factor} \leq 2.0$, and an extended source when $Y_{factor} > 2.0$. In Fig. 13, we plot the Y-factor distribution of the GLOSTAR sources. Similarly, Fig. 14 shows the distribution of source effective radius. Both results show that our catalog mainly comprises compact and unresolved sources.

5.3. Spectral indices

Sources that exhibit radio emission produced from ionized thermal gas with temperature $> 10^4$ K (such as H II regions and PNe) have spectral indices ranging from –0.1 to 2.0, representing optical thin and thick bremsstrahlung, respectively. On the other hand, non-thermal radio emission is produced in high-energy processes. The most common, resulting in synchrotron radiation, is produced by relativistic electrons spiralling around magnetic field lines and reaches brightness temperatures above 10^6 K. Active galactic nuclei, for example, are common nonthermal radio emitters. Other compact Galactic nonthermal radio sources are pulsars (PSRs) and micro-quasars. Interestingly, also in the star formation context nonthermal radio emission may arise from compact sources, such as strong wind collision regions in massive multiple stellar systems (Dzib et al. 2013; Yanza et al. Submitted.), strong shocks of jets of very young massive stars (Reid et al. 1995; Carrasco-González et al. 2010), and magnetically active young low-mass stars (Forbrich et al. 2021; Dzib et al. 2021). Typical spectral index values for non-thermal radio sources related to massive stars are about –0.5 (e.g., Reid et al.
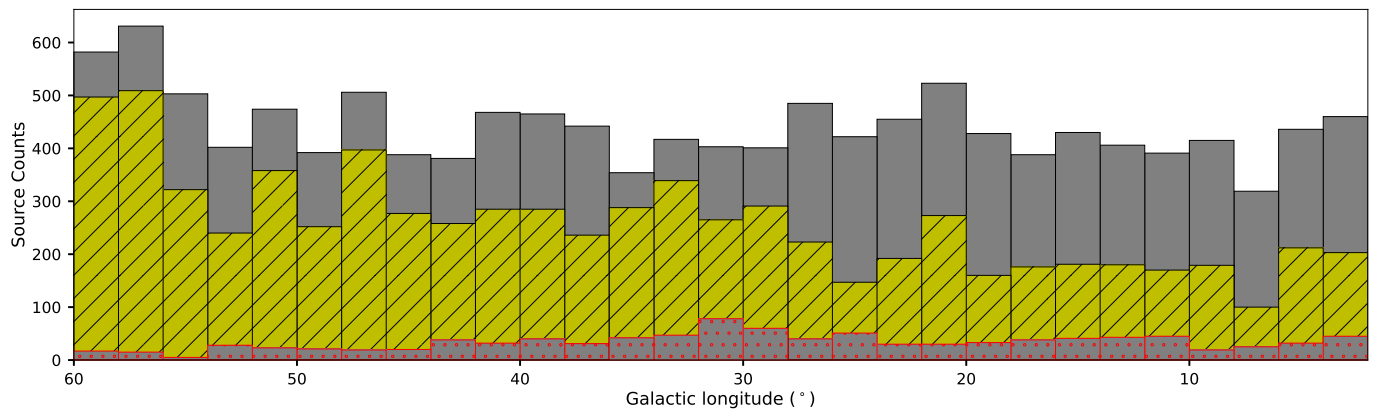
Fig. 10. Source distribution of GLOSTAR D-configuration sources in Galactic longitude. Sources in the range $28° < \ell < 36°$ are taken from Medina et al. (2019). The color of the bars is the same as for Fig. 9. The bin size is $2°$.

Fig. 11. Spatial distribution of GLOSTAR radio sources reported in this work. Different markers are used for the different resulting source classifications and are labeled on the right side of the plot. Squares delimit the the area of the large scale structures also identified in this work (see Sec. 3.2). Sources in the range $28° < \ell < 36°$ are taken from Medina et al. (2019).

1995; Dougherty et al. 2003; Mohan et al. 2022). However, the spectral index of radio emission from magnetically active stars ranges from −2.0 to +2.0 (Dulk 1985; Dzib et al. 2015).

In this work, we have measured the spectral index of over 5 000 sources. First, by using the upgraded capabilities of the VLA interferometer that offer a total bandwidth of 4 GHz in C-band, we have produced images in smaller frequency bins and determined *in-band* spectral indices of compact sources detected with S/N ratio > 10.0. Second, we have used the flux densities from the THOR survey and computed GLOSTAR-THOR spec-

tral indices of compact sources detected in both surveys. Using the flux densities reported by THOR has two advantages. First, it increases the frequency baseline of the spectral index determination. Second, the total flux densities of both surveys can be used without splitting the data into smaller and less sensitive frequency bins. By using the full-band images of both surveys, we optimize the (u, v)-coverage of both surveys. This results in smaller errors in the spectral index determination. Quantitatively, this is reflected by the fact that we obtain mean error values for the in-band and the GLOSTAR-THOR spectral indices of

Fig. 13. Distribution of Y-factor of GLOSTAR sources. The red ($Y_{factor} = 1.2$) and cyan ($Y_{factor} = 2.0$) dashed-dotted lines indicate the criterion used to distinguish between unresolved, compact, and extended sources, respectively. The bin width is 0.05 dex.

Fig. 12. Peak (top) and integrated (bottom) flux distribution of GLOSTAR sources. The blue and yellow dashed lines in the upper panel delimit the $4\sigma_{noise}$ detection limit in areas free of extended emission ($\sigma_{noise} \simeq 50\mu$Jy beam^{-1}) and for the nominal noise level of the D-configuration images ($\sigma_{noise} \simeq 123\mu$Jy beam^{-1}). The red histogram in the upper panel shows the flux distribution of sources previously identified by CORNISH. The bin width is 0.1 dex.

Fig. 14. Distribution of the source radii. The dashed red line indicates the resolution of the observation (radius of the synthesized beam). The bin size used is 0.05 dex.

0.2 and 0.07, respectively. We also notice the recent findings by Rashid et al. (2024), whose results indicate that broadband spectral indices are more reliable than in-band spectral indices. For the 2 819 sources in which both spectral indices could be determined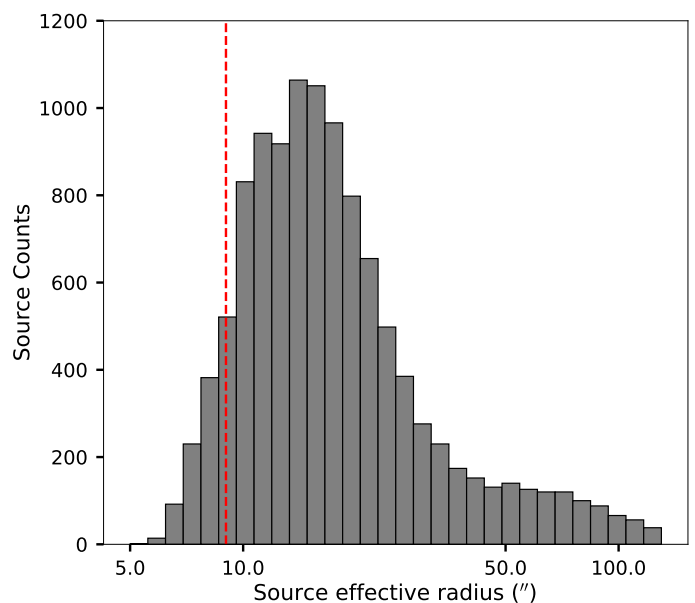, we plot their values in the top panel of Fig. 15. In the middle panel of Fig. 15 we show the distribution of the differences between these two spectral index determinations, and in the low panel we plot this difference against the GLOSTAR source effective radius. We found a mean difference of -0.08 ± 0.01 and a standard deviation of 0.35. To check if the small negative difference is correlated with size, we ran a Pearson correlation test between the source effective radius and the difference of spectral indices. We obtain a correlation coefficient $r = -0.14$, with

a significance value of $p = 6 \times 10^{-14}$. This indicates a weak negative correlation (larger sources have more negative values) and could explain the small negative difference between the two spectral index determinations. While the in-band spectral indices are slightly more negative than the GLOSTAR-THOR spectral index, the independent spectral index determinations are consistent considering the mean values of the errors obtained for both methods. Because the error bars are smaller, however, a preference is given to the GLOSTAR-THOR spectral indices.

Figure 16 shows the GLOSTAR-THOR spectral index distribution of GLOSTAR sources. The distribution shows two peaks, the first at a value ~ -0.6 and the second at a value ~ 0.0, point-

Fig. 16. GLOSTAR-THOR spectral index distribution of radio sources reported in this work. In gray is the full sample, yellow is for sources related to EgC and red for H ɪɪ region candidates. The histogram used a bin size of 0.1.

sources (yellow histogram) shows only one peak and the mean is ~ -0.6, similar to the canonical value of -0.7 for extragalactic nonthermal radio sources (Condon 1984). For the 225 H ɪɪ regions with measured spectral index (red histogram), the distribution also shows a single peak at $\alpha = 0.14 \pm 0.02$, consistent with the values for (almost) optically thin free-free emission (thermal radio emission). We will discuss H ɪɪ regions in more detail in the following section.

5.4. H ɪɪ regions

Following the classification criteria discussed in Section 4.6, we have identified 769 H ɪɪ regions, of which 359 are new H ɪɪ region candidates. Most of them are located close to the mid-plane of the Galactic disk ($b \simeq 0.0$, see Figure 9). Most of the newly identified H ɪɪ region candidates are compact, with an effective radius smaller than 20″ (see Fig. 17).

We have estimated the spectral index for 225 H ɪɪ region candidates, and their mean spectral index value is $+0.14 \pm 0.02$ (Fig. 16). Surprisingly, 55 (24%) of the H ɪɪ region candidates have a spectral index < -0.2, which is smaller than -0.1, the minimum spectral index value expected for optically thin free-free radio emission. In the GLOSTAR higher angular resolution images, we have also found such sources (Dzib et al. 2023; Yang et al. 2023). In those cases, we have speculated that in H ɪɪ regions associated with radio sources with negative spectral indices, the radio sources do not trace radio emission from the ionized gas of the H ɪɪ region, which will be resolved out, but rather trace stellar processes producing non-thermal radio emission or a mixture of emission produced by thermal and non-thermal processes. Sensitive radio observations have indeed revealed compact non-thermal radio sources in the vicinity of the H ɪɪ regions proper, up to several tens in some cases (e.g., Wilner et al. 1999; Medina et al. 2018; Yanza et al. 2022). Wilner et al. (1999) argue that the non-thermal compact radio sources they find around the archetypal ultracompact H ɪɪ region W3(OH), several of which

Fig. 15. Comparison of GLOSTAR in-band and GLOSTAR-THOR spectral indices. *Top:* Scatter plot of α_{Inband} vs. $\alpha_{\mathrm{GLOSTAR-THOR}}$. The dashed black line is the equality line. *Middle:* Distribution of the differences of the spectral indices. The yellow dashed line indicates the mean value of -0.08 ± 0.01. The standard deviation is 0.35. The histogram used a bin size of 0.1. *Bottom:* Source effective radius vs. $\alpha_{\mathrm{Inband}} - \alpha_{\mathrm{GLOSTAR-THOR}}$.

ing to two populations of radio sources. The distribution of EgC

Fig. 17. Distribution of H ɪɪ region effective radius. The grey bars show the distribution for all identified H ɪɪ regions. Red bars are the new H ɪɪ regions candidates identified in this work. The dashed yellow line indicates the resolution of the observation (radius of the synthesized beam). The bin size used is 0.05 dex.

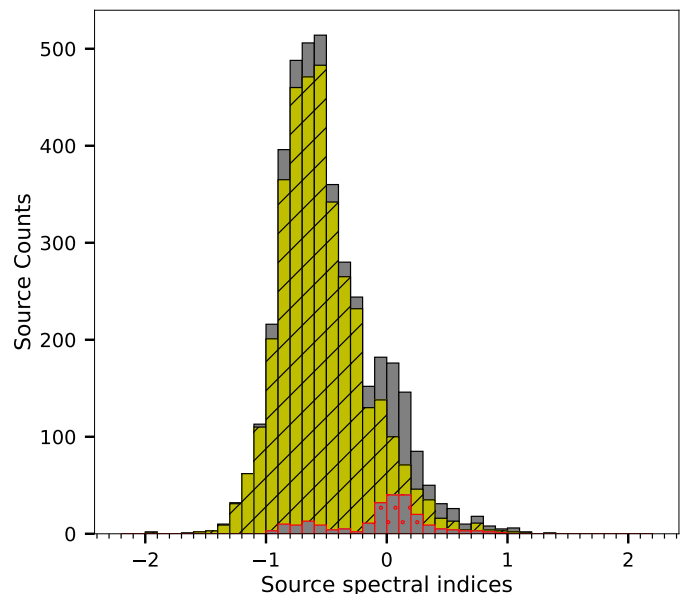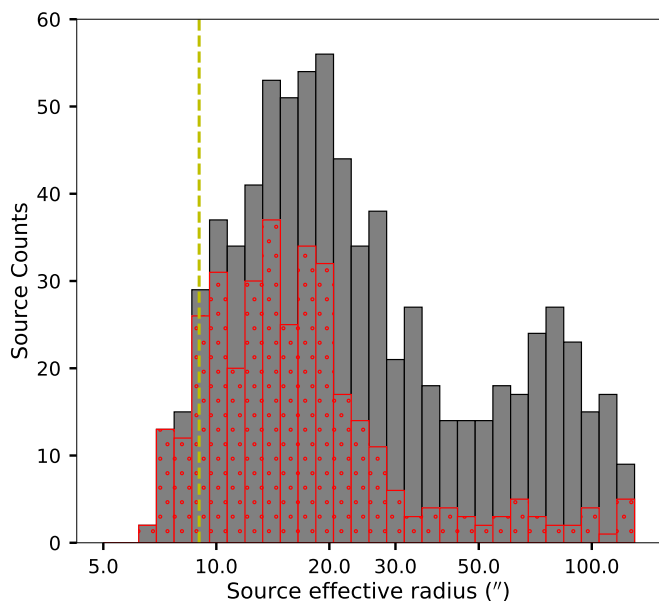**Fig. 18.** Spectral indices of H ɪɪ regions as a function of the S/N. The circles are color-coded with their S/N in the THOR survey. The dashed line shows the spectral index value of –0.1, the minimum expected for optically thin free-free radio emission.

are time variable, represent low-mass stars in the stellar cluster that surrounds the MYSO that excites the H ɪɪ region.

In our VLA D-configuration images, we do not expect that H ɪɪ regions related to compact radio sources ($Y_{factor} \leq 2.0$) have resolved out emission. This excludes the possibility of imaging artifacts.

In Fig. 18 we plot the 225 spectral indices measured for H ɪɪ region candidates as a function of their signal-to-noise ratio from the GLOSTAR maps. From this plot, it can be seen that most of the sources with negative spectral index also have a low S/N ratio. Most of them also have a low S/N ratio in the THOR survey. The low brightness of these sources could have biased the spectral index determination. However, there are still some sources with a S/N ratio >10 in both GLOSTAR and THOR, that clearly have a negative spectral index. These radio sources require further studies to confirm or refute their classification as H ɪɪ regions.

5.5. Extragalactic background sources

Along with Galactic sources, our observations are expected to detect a large number of extragalactic radio sources. In fact, it has been shown that most of the unclassified sources in our previous catalog can indeed be related to galaxies with radio emission (Medina et al. 2019; Chakraborty et al. 2020). While selections effects could play a role on their distribution, the early studies by Fomalont et al. (1991) show that, at 5 GHz, the rough number of expected background sources per square arcminute, with flux levels above $S\,[\mu Jy]$, is described by:

$$N(S\,[\mu Jy]) = (0.42 \pm 0.05)(S\,[\mu Jy]/30)^{-1.18\pm0.19}.$$

Considering a mean noise level of σ =123 μJy, and a 4 σ threshold for our detected sources, the number of expected extragalactic radio sources in our images is 6 400 ± 3 750. This number is in excellent agreement with the 6 312 sources that we have classified as EgC.
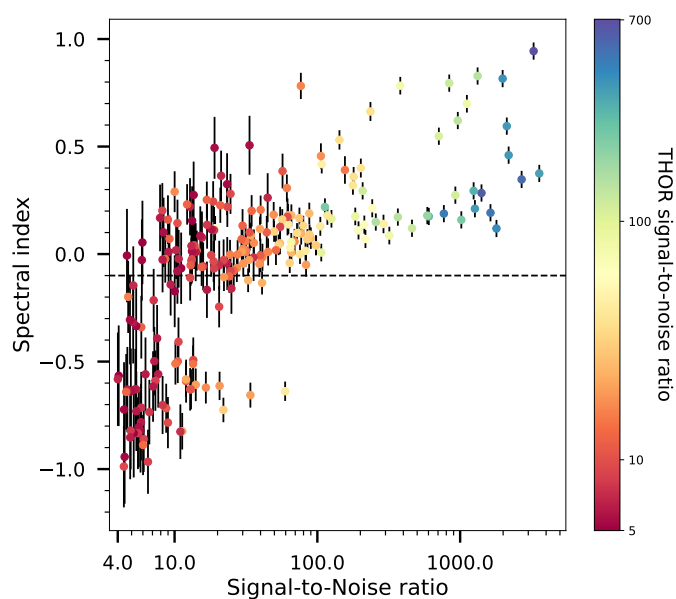
6. Summary and Conclusions

The GLOSTAR-VLA Galactic plane survey (Medina et al. 2019; Brunthaler et al. 2021) is currently the most sensitive mid-radio wavelength survey covering a large fraction of the Galactic plane observed from the northern hemisphere. Its main objective is unveiling signatures of recent massive star formation. However, as many of these sources are expected to be extragalactic background sources, it is necessary to classify the detected sources, a task that has many challenges.

In this work, we have presented radio images of a 100 square degree area of the Galactic plane, with an angular resolution of 18″. The mapped region covers the area delimited by the coordinates $2° < \ell < 28°$, $36° < \ell < 60°$ and $|b| < 1°$. We have used a combination of the BLOBCAT software and visual inspection procedures to identify 11 211 radio sources in the GLOSTAR map. We have identified 1 965 that are part of very extended sources (H ɪɪ region complexes or SNRs). The radio source catalog presents the results of the source extraction performed with BLOBCAT, such as positions, S/N, flux densities, Y-factor, and effective radius. We have also obtained the spectral indices of 5 276 radio sources, which are also listed in the catalog. We have cross-matched the GLOSTAR radio sources with the radio sources reported from other radio surveys; for example, THOR (Beuther et al. 2016), CORNISH (Hoare et al. 2012), and RMS (Urquhart et al. 2009). These radio surveys were used to, first, verify the measured source parameters and, second, to classify sources. Source classification was also performed with the information on (sub)millimeter and IR wavelength counterparts. Source classes are also listed in the catalog, in which a large number (6 312) are extragalactic background sources.

With the performed multi-wavelength analysis, we identified 769 H ɪɪ region candidates. Previous works have reported 410 of these as H ɪɪ regions or H ɪɪ region candidates, and the remaining 359 we identify as H ɪɪ candidates for the first time. The spatial distribution of these sources is concentrated around the Galactic mid-plane and their numbers decrease in the outer parts of

the Galactic disk ($\ell > 56°$), indicating zones with higher and lower star formation, respectively. Using additional flux density measurements at 1.4 GHz from the THOR survey, we have also determined spectral indices of 225 H ɪɪ region candidates. Their mean spectral index is ∼ 0.1, consistent with thermal free-free radio emission. Interestingly we found several H ɪɪ region candidates with negative spectral index, although this could be partly due to their low S/N ratio in GLOSTAR and THOR. However, there is an interesting sample of H ɪɪ region candidates with S/N>10 and negative spectral indices that need to be studied further to establish their true nature.

Combining the information from large surveys is an excellent way to obtain an unbiased look for tracers of early star formation. The derived properties and classification of several thousands of new and known radio sources are invaluable information and truly show the legacy nature of the GLOSTAR radio survey.

References

Anderson, L. D., Bania, T. M., Balser, D. S., et al. 2014, ApJS, 212, 1
Anderson, L. D., Wang, Y., Bihr, S., et al. 2017, A&A, 605, A58
Anderson, L. D., Zavagno, A., Barlow, M. J., García-Lario, P., & Noriega-Crespo, A. 2012, A&A, 537, A1
Bertin, E. & Arnouts, S. 1996, A&AS, 117, 393
Beuther, H., Bihr, S., Rugel, M., et al. 2016, A&A, 595, A32
Brunthaler, A., Menten, K. M., Dzib, S. A., et al. 2021, A&A, 651, A85
Carrasco-González, C., Rodríguez, L. F., Anglada, G., et al. 2010, Science, 330, 1209
Chakraborty, A., Roy, N., Wang, Y., et al. 2020, MNRAS, 492, 2236
Chini, R. & Hoffmeister, V. 2008, in Handbook of Star Forming Regions, Volume II, ed. B. Reipurth, Vol. 5, 625
Churchwell, E., Babler, B. L., Meade, M. R., et al. 2009, PASP, 121, 213
Condon, J. J. 1984, ApJ, 287, 461
Contreras, Y., Schuller, F., Urquhart, J. S., et al. 2013, A&A, 549, A45
Cotton, W. D. 2008, PASP, 120, 439
Csengeri, T., Urquhart, J. S., Schuller, F., et al. 2014, A&A, 565, A75
Dokara, R., Brunthaler, A., Menten, K. M., et al. 2021, A&A, 651, A86
Dokara, R., Gong, Y., Reich, W., et al. 2023, A&A, 671, A145
Dougherty, S. M., Pittard, J. M., Kasian, L., et al. 2003, A&A, 409, 217
Dulk, G. A. 1985, ARA&A, 23, 169
Dzib, S. A., Forbrich, J., Reid, M. J., & Menten, K. M. 2021, ApJ, 906, 24
Dzib, S. A., Loinard, L., Rodríguez, L. F., et al. 2015, ApJ, 801, 91
Dzib, S. A., Rodríguez, L. F., Loinard, L., et al. 2013, ApJ, 763, 139
Dzib, S. A., Yang, A. Y., Urquhart, J. S., et al. 2023, A&A, 670, A9

Elia, D., Merello, M., Molinari, S., et al. 2021, MNRAS, 504, 2742
Elia, D., Molinari, S., Schisano, E., et al. 2017, MNRAS, 471, 100
Fazio, G. G., Hora, J. L., Allen, L. E., et al. 2004, ApJS, 154, 10
Fomalont, E. B., Windhorst, R. A., Kristian, J. A., & Kellerman, K. I. 1991, AJ, 102, 1258
Forbrich, J., Dzib, S. A., Reid, M. J., & Menten, K. M. 2021, ApJ, 906, 23
Ghosh, S. K., Iyengar, K. V. K., Rengarajan, T. N., et al. 1989, ApJ, 347, 338
Ginsburg, A., Goddi, C., Kruijssen, J. M. D., et al. 2017, ApJ, 842, 92
Gong, Y., Ortiz-León, G. N., Rugel, M. R., et al. 2023, A&A, 678, A130
Green, D. A. 2019, Journal of Astrophysics and Astronomy, 40, 36
Green, J. A., Caswell, J. L., Fuller, G. A., et al. 2009, MNRAS, 392, 783
Greisen, E. W. 2003, in Astrophysics and Space Science Library, Vol. 285, Information Handling in Astronomy - Historical Vistas, ed. A. Heck, 109
Hales, C. A., Murphy, T., Curran, J. R., et al. 2012, MNRAS, 425, 979
Helfand, D. J., Becker, R. H., White, R. L., Fallon, A., & Tuttle, S. 2006, AJ, 131, 2525
Hoare, M. G., Lumsden, S. L., Oudmaijer, R. D., et al. 2005, in Massive Star Birth: A Crossroads of Astrophysics, ed. R. Cesaroni, M. Felli, E. Churchwell, & M. Walmsley, Vol. 227, 370–375
Hoare, M. G., Purcell, C. R., Churchwell, E. B., et al. 2012, PASP, 124, 939
Holwerda, B. W. 2005, ArXiv Astrophysics e-prints [`astro-ph/0512139`]
Irabor, T., Hoare, M. G., Oudmaijer, R. D., et al. 2018, MNRAS, 480, 2423
Kerton, C. R., Arvidsson, K., & Alexander, M. J. 2013, AJ, 145, 78
Khan, S., Rugel, M. R., Brunthaler, A., et al. 2024, arXiv e-prints, arXiv:2407.05770
Lucas, P. W., Hoare, M. G., Longmore, A., et al. 2008, MNRAS, 391, 136
Lumsden, S. L., Hoare, M. G., Urquhart, J. S., et al. 2013, ApJS, 208, 11
Marleau, F. R., Noriega-Crespo, A., Paladini, R., et al. 2008, AJ, 136, 662
Medina, S. N. X., Dzib, S. A., Tapia, M., Rodríguez, L. F., & Loinard, L. 2018, A&A, 610, A27
Medina, S. N. X., Urquhart, J. S., Dzib, S. A., et al. 2019, A&A, 627, A175
Messineo, M., Davies, B., Figer, D. F., et al. 2011, ApJ, 733, 41
Mohan, S., Vig, S., & Mandal, S. 2022, MNRAS, 514, 3709
Molinari, S., Schisano, E., Elia, D., et al. 2016, A&A, 591, A149
Molinari, S., Swinyard, B., Bally, J., et al. 2010, A&A, 518, L100
Motte, F., Bontemps, S., & Louvet, F. 2018, ARA&A, 56, 41
Nguyen, H., Rugel, M. R., Menten, K. M., et al. 2021, A&A, 651, A88
Nguyen, H., Rugel, M. R., Murugeshan, C., et al. 2022, A&A, 666, A59
Oliveira, J. M. 2008, in Handbook of Star Forming Regions, Volume II, ed. B. Reipurth, Vol. 5, 599
Ortiz-León, G. N., Menten, K. M., Brunthaler, A., et al. 2021, A&A, 651, A87
Purcell, C. R., Hoare, M. G., Cotton, W. D., et al. 2013, ApJS, 205, 1
Rashid, M., Roy, N., Pandian, J. D., et al. 2024, arXiv e-prints, arXiv:2405.18978
Reid, M. J., Argon, A. L., Masson, C. R., Menten, K. M., & Moran, J. M. 1995, ApJ, 443, 238
Schuller, F., Menten, K. M., Contreras, Y., Wyrowski, F., & Schilke, e. a. 2009, A&A, 504, 415
Urquhart, J. S., Busfield, A. L., Hoare, M. G., et al. 2007, A&A, 461, 11
Urquhart, J. S., Csengeri, T., Wyrowski, F., et al. 2014, A&A, 568, A41
Urquhart, J. S., Hoare, M. G., Purcell, C. R., et al. 2009, A&A, 501, 539
Urquhart, J. S., König, C., Giannetti, A., et al. 2018, MNRAS, 473, 1059
Urquhart, J. S., Thompson, M. A., Moore, T. J. T., et al. 2013, MNRAS, 435, 400
Urquhart, J. S., Wells, M. R. A., Pillai, T., et al. 2022, MNRAS, 510, 3389
Wang, Y., Beuther, H., Rugel, M. R., et al. 2020, A&A, 634, A83
Wang, Y., Bihr, S., Rugel, M., et al. 2018, A&A, 619, A124
Wilner, D. J., Reid, M. J., & Menten, K. M. 1999, ApJ, 513, 775
Wright, E. L., Eisenhardt, P. R. M., Mainzer, A. K., et al. 2010, AJ, 140, 1868
Yang, A. Y., Dzib, S. A., Urquhart, J. S., et al. 2023, A&A, 680, A92
Yang, A. Y., Urquhart, J. S., Thompson, M. A., et al. 2021, A&A, 645, A110
Yanza, V., Dzib, S. A., Palau, A., et al. Submitted., MNRAS, XXX, YY
Yanza, V., Masqué, J. M., Dzib, S. A., et al. 2022, AJ, 163, 276
Zhang, B., Reid, M. J., Zhang, L., et al. 2019, AJ, 157, 200